

Last Layer Hamiltonian Monte Carlo

Koen Vellenga

*Volvo Car Corporation
SAIL, University of Skövde*

H. Joe Steinhauer

SAIL, University of Skövde

Göran Falkman

SAIL, University of Skövde

Jonas Andersson

Volvo Car Corporation

Anders Sjögren

Volvo Car Corporation

Abstract

We explore the use of Hamiltonian Monte Carlo (HMC) sampling as a probabilistic last layer approach for deep neural networks (DNNs). While HMC is widely regarded as a gold standard for uncertainty estimation, the computational demands limit its application to large-scale datasets and large DNN architectures. Although the predictions from the sampled DNN parameters can be parallelized, the computational cost still scales linearly with the number of samples (similar to an ensemble). Last layer HMC (LL-HMC) reduces the required computations by restricting the HMC sampling to the final layer of a DNN, making it applicable to more data-intensive scenarios with limited computational resources. In this paper, we compare LL-HMC against five last layer probabilistic deep learning (LL-PDL) methods across three real-world video datasets for driver action and intention. We evaluate the in-distribution classification performance, calibration, and out-of-distribution (OOD) detection. Due to the stochastic nature of the probabilistic evaluations, we performed five grid searches for different random seeds to avoid being reliant on a single initialization for the hyperparameter configurations. The results show that LL-HMC achieves competitive in-distribution classification and OOD detection performance. Additional sampled last layer parameters do not improve the classification performance, but can improve the OOD detection. Multiple chains or starting positions did not yield consistent improvements. Implementation is available at: <https://github.com/koenvellenga/LL-HMC/>.

1 Introduction

The rapid progress in Artificial Intelligence (AI) has amplified the need for robust and transparent decision making (Hendrycks et al., 2021; Papamarkou et al., 2024; Bengio et al., 2024; Manchingal & Cuzzolin, 2025). When using deep neural networks (DNN) in safety-critical environments, it is important that the model is able to identify instances it cannot confidently predict. Regular DNNs are unable to express uncertainty about their outputs, suffer from opaque decision-making processes (Rudin, 2019), can be poorly calibrated (Guo et al., 2017; Nixon et al., 2019), struggle with noisy sensor observations (Berrada et al., 2021), require explicit safety verification (Wang et al., 2024b), and perform poorly on long-tail edge cases (Hendrycks et al., 2021). To address the lack of uncertainty estimation in regular DNNs, various methods have been proposed (e.g., Neal 1996; Shafer & Vovk 2008; Welling & Teh 2011; Hoffman et al. 2013; Gal & Ghahramani 2016; Maddox et al. 2019; Van Amersfoort et al. 2020; Wilson & Izmailov 2020; Franchi et al. 2024). Hamiltonian

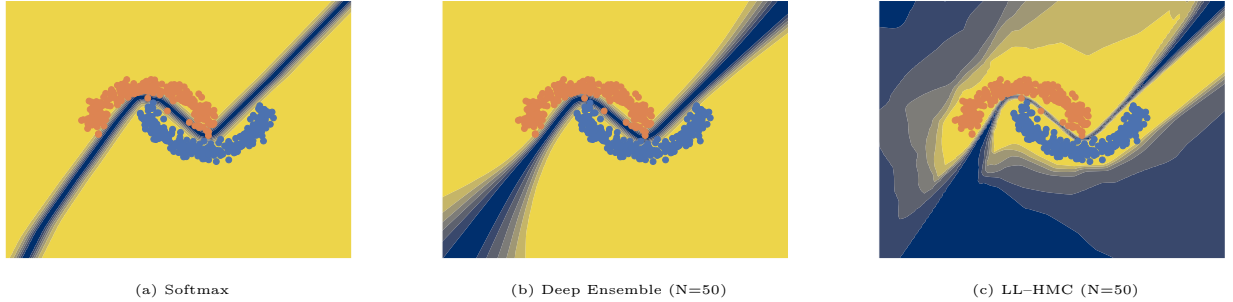


Figure 1: Uncertainty estimation example for the two moons toy dataset for a softmax, deep ensemble, and the last layer Hamiltonian Monte-Carlo methods. Yellow indicates certain areas, dark blue indicates uncertain areas (the color maps are normalized.).

Monte-Carlo (HMC) sampling is often regarded as the gold standard for uncertainty quantification and can yield top performance (Izmailov et al., 2021). However, HMC can become too computationally expensive to estimate the uncertainty when scaling to bigger datasets and larger DNN architectures.

In machine learning it is common to decompose uncertainty into aleatoric uncertainty (randomness in the process) and epistemic uncertainty (the lack of knowledge) (Der Kiureghian & Ditlevsen, 2009). Distinguishing between these two uncertainty types can help to identify the potentially reducible epistemic uncertainty (Hüllermeier & Waegeman, 2021). In practice, it is challenging to decouple these uncertainty types (Mucsányi et al., 2024). However, the predictive uncertainty (the aleatoric and epistemic uncertainty combined) can be used to evaluate, for example, whether a model expresses higher uncertainty for out-of-distribution (OOD) instances. The effectiveness of the predictive uncertainty depends on how well a probabilistic approach captures the underlying uncertainty. In classification tasks, the predictive distribution (e.g., softmax output) is sometimes assumed to be sufficient for identifying OOD instances. However, the softmax distribution is commonly only uncertain along the decision boundaries (Van Amersfoort et al., 2020), which limits its use for detecting unseen or ambiguous inputs (see Figure 1). Similarly, an ensemble improves the uncertainty estimations for regions where it has not observed any data compared to a single softmax-based uncertainty estimation. However, the ensemble mostly remains uncertain along the decision boundary. Additionally, the ensemble scales linearly with the number of ensemble members in terms of required computational resources to produce the estimations.

Especially for safety-critical tasks that operate in a resource-constrained environment, we require efficient approaches to produce uncertainty estimates. Driving automation is an example safety-critical application domain with limited onboard computational resources, which requires continuous perception and decision-making under uncertainty. An example of a driving automation task is to accurately recognize the current actions and intentions of a driver to avoid future traffic conflicts. For such a human behavior application, estimating uncertainties and understanding the limitations of a model are essential. Therefore, in this paper we explore confining HMC sampling to the last layer of a DNN as an efficient probabilistic deep learning (PDL) approach. We evaluate last layer HMC (LL-HMC) on three driver action and intention recognition video datasets. We compare the classification performance and uncertainty-based OOD detection of LL-HMC to a deterministic softmax baseline, an ensemble, and five other probabilistic last layer approaches.

2 Related Work

2.1 Probabilistic Deep Learning

We provide a high-level explanation of a selection of PDL methods. For a comprehensive overview of Bayesian, PDL or stochastic approaches, refer to one of the following papers: Zhou et al. (2022); Jospin et al. (2022); Arbel et al. (2023); Gawlikowski et al. (2023); Papamarkou et al. (2024); Manchingal & Cuzzolin (2025). Markov Chain Monte Carlo (MCMC) can be used to estimate the posterior distribution of a DNN’s parameters through sampling. Unlike optimization methods, which adjust the model’s parameters by calculating the

gradient of the loss function to find a local minimum, MCMC samples from the parameter space using probabilistic inference. Bayes’ theorem ($p(\theta|D) = \frac{p(D|\theta)p(\theta)}{p(D)}$) plays a crucial role in this process, where θ represents the DNN parameters, D is the evidence, $p(\theta)$ the prior probability of the parameters before considering the evidence, and $p(D|\theta)$ the likelihood of the evidence given the parameters. MCMC algorithms begin by selecting an initial value for each parameter and aim to explore the entire parameter space. An example of an informed MCMC sampler is the HMC algorithm (Neal, 1992; Neal et al., 2011), which leverages gradient information and principles from Hamiltonian dynamics to efficiently navigate the parameter space. The sampler proposes new parameter values and calculates the likelihood of the dataset given both the new and current parameter positions to evaluate the proposal. By dividing these probabilities, we obtain an acceptance ratio, allowing us to compare the full posterior probabilities at two different points without knowing their exact values. This comparison guides the algorithm to sample more frequently from regions with high posterior probability and less frequently from regions with low probability.

For HMC, the No U-Turn Sampler (NUTS) dynamically adjusts the number of steps taken by the integrator to ensure an optimal length for the Hamiltonian trajectory (Hoffman et al., 2014). Consequently, the HMC sampler can explore the parameter space efficiently by concentrating on more probable regions of the posterior. Initially, the samples generated by the Markov Chain may be far from the true target distribution, necessitating a burn-in period to ensure convergence to the posterior distribution $p(\theta|D)$. Once convergence is achieved, the samples produced by the Markov Chain can be stored and used for making predictions on the test data (Geyer, 2011; Betancourt, 2017; Jospin et al., 2022). Izmailov et al. (2021) applied HMC to larger datasets and architectures, but required substantial computational resources. While there have been examples of either pre-training (Benker et al., 2021; Vellenga et al., 2024a), chain-splitting (Cobb & Jalaian, 2021) or stochastic gradient MCMC (Chen et al., 2014; Zhang et al., 2020) to enable using HMC without significantly scaling the required computational resources, it remains challenging to use HMC sampling for large DNN architectures and big datasets.

Due to the computational demands of MCMC, alternative approaches like stochastic variational inference (SVI) have gained popularity for approximating posterior distributions of DNNs more efficiently. Variational inference (VI) aims to estimate the intractable posterior distribution through replacing the parameters of a DNN with a set of variational distributions q . A common approach for VI is to replace each network parameter as a 1-dimensional Gaussian distribution. To approximate the true (intractable) posterior distribution, the evidence lower bound (ELBO) (Jordan et al., 1999; Blei et al., 2017) is used to minimize the Kullback-Leibler (KL) divergence between the variational distribution and the true posterior. Since backpropagating through randomly sampled variables (the variational distributions q) is infeasible, Bayes-by-backprop (BBB, Blundell et al. 2015) employs the reparameterization trick (Kingma & Welling, 2014). The introduction of a new variable $\epsilon \sim \mathcal{N}(0, 1)$ reparameterizes the random variable q , which allows the sampling process to be differentiable and thus facilitates the backpropagation.

Uncertainty can also be estimated by an ensemble of DNNs, which requires no assumptions about the posterior distribution. A Deep Ensemble (DE) (Lakshminarayanan et al., 2017) consists of multiple independently trained DNNs with random initializations, and tend to produce a diverse set of model parameters (Ashukha et al., 2020; Abe et al., 2022; Laurent et al., 2024). However, a key limitation of sequential sampling approaches (e.g., BBB), MCMC or ensembles, is that they scale linearly to produce predictions and thus uncertainty estimations. This requires additional computations, which can be a burden for deployment in a resource-constrained safety-critical operating environment. Given the scalability limitations, more efficient sampling-free PDL approaches have been proposed. Sampling-free PDL methods do not rely on, for example, sampling the DNN parameters when estimating predictive uncertainty. An example of a distance-based sampling-free approach is Deep Deterministic Uncertainty (DDU) (Mukhoti et al., 2023). DDU applies Gaussian Discriminant Analysis to the spectrally normalized feature space of a pre-trained DNN. DDU has demonstrated effectiveness on image classification OOD benchmarks. Packed-ensembles (PE) (Laurent et al., 2023) combine multiple sub-networks into a deterministic model by using grouped convolutions. This allows training multiple sub-networks simultaneously.

Complementing the more efficient PDL approaches, it is also possible to restrict the stochastic component to the last layer of a DNN (Snoek et al., 2015; Watson et al., 2021). For example, Variational Bayes Last Layer (VBLL) (Harrison et al., 2024) performs variational inference over the parameters of the final layer.

VBLL uses approximate analytic expression for the variational lower bound of the marginal likelihood, which eliminates the need for stochastic sampling. A Sub-Ensemble (SE) (Valdenegro-Toro, 2023) is an ensemble of independently trained classifiers instead of entire DNNs. BBB, and PE can also be applied to the final layer of a DNN to produce uncertainty estimations. Altogether, while these previous PDL approaches demonstrated efficient approximation of the posterior, they potentially fall short compared to MCMC-based approaches. An oversimplification of the true posterior can lead to over or underconfident uncertainty estimates, whereas HMC sampling can capture complex multi-modal distributions that are (highly) non-Gaussian.

2.2 Driver action and intention recognition

Given the continued presence of human-driven vehicles on the road, an important aspect of driving automation is to understand human behavior in traffic scenarios. An example of an advanced driver assistance system (ADAS) is to assess whether the intended maneuvers of a driver are safe to execute for a particular driving scene. Central components of such an ADAS are driver action and intention recognition. Actions refer to the observable behaviors a driver performs, such as steering, braking, or changing lanes, which can be directly captured through various sensors on a vehicle. Intention recognition focuses on identifying what a driver plans to do in the immediate future, before the actual maneuver takes place (Pereira et al., 2013; Sadri, 2011). For example, before changing lanes, a driver might form the intention several seconds before executing any observable actions of that intended driving maneuver. Understanding both actions and intentions is crucial for developing an ADAS that can anticipate and respond to driver behavior (Vellenga et al., 2022).

Previous studies on driving action recognition (DAR) and driver intention recognition (DIR) have explored various approaches to model the sequential spatio-temporal relationships captured by various sensors. For example, Yang et al. (2023) demonstrated DAR performance improvements when fusing extracted facial landmarks of the ego-vehicle driver and end-to-end representations from three exterior video streams and one in-cabin video streams. Noguchi & Tanizawa (2023) constructed spatial-temporal graphs based on exterior-based object detection and tracking, employing a semi-supervised contrastive learning framework to train a graph convolutional network. For end-to-end DIR, Gebert et al. (2019) extracted the optical flow of the in-cabin videos, whereas Rong et al. (2020) extracted and predicted the optical flow for the exterior cameras. Vellenga et al. (2024b) fine-tuned video masked auto-encoders and attention fusion to improve DAR and DIR performance. Although these DAR and DIR approaches have incrementally improved performance, they have not considered the uncertainty-based OOD detection, which is a critical aspect for safe driving automation.

2.3 Driver action and intention recognition

Given the continued presence of human-driven vehicles on the road, an important aspect of driving automation is to understand human behavior in traffic scenarios. An example of an advanced driver assistance system (ADAS) is to assess whether the intended maneuvers of a driver are safe to execute for a particular driving scene. Central components of such an ADAS are driver action and intention recognition. Actions refer to the observable behaviors a driver performs, such as steering, braking, or changing lanes, which can be directly captured through various sensors on a vehicle. Intention recognition focuses on identifying what a driver plans to do in the immediate future, before the actual maneuver takes place (Pereira et al., 2013; Sadri, 2011). For example, before changing lanes, a driver might form the intention several seconds before executing any observable actions of that intended driving maneuver. Understanding both actions and intentions is crucial for developing an ADAS that can anticipate and respond to driver behavior (Vellenga et al., 2022).

Previous studies on driving action recognition (DAR) and driver intention recognition (DIR) have explored various approaches to model the sequential spatio-temporal relationships captured by various sensors. For example, Yang et al. (2023) Yang et al. (2023) demonstrated DAR performance improvements when fusing extracted facial landmarks of the ego-vehicle driver and end-to-end representations from three exterior video streams and one in-cabin video streams. Noguchi and Tanizawa (2023) Noguchi & Tanizawa (2023) constructed spatial-temporal graphs based on exterior-based object detection and tracking, employing a semi-supervised contrastive learning framework to train a graph convolutional network. For end-to-end DIR, Gebert et al. (2019) Gebert et al. (2019) extracted the optical flow of the in-cabin videos, whereas Rong et al.

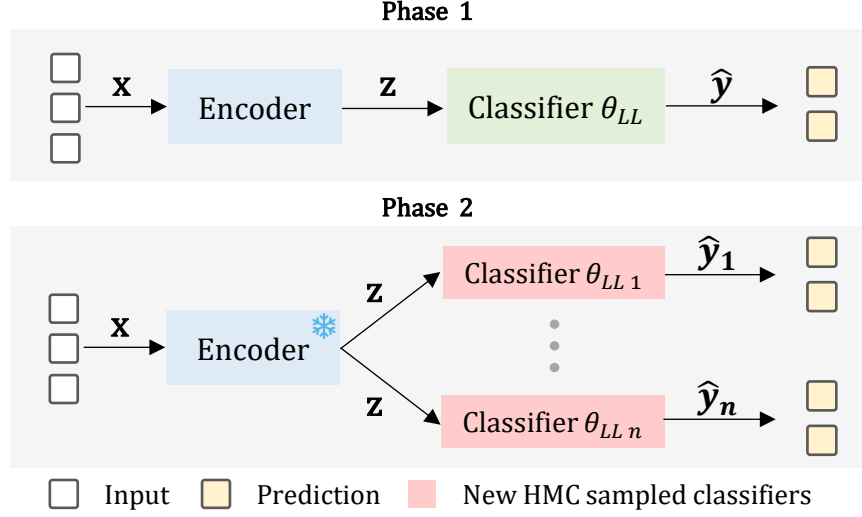


Figure 2: Schematic overview of the two last layer HMC phases. Phase 1 covers the regular optimization-based training phase. During phase 2, the frozen pre-trained encoder is responsible for extracting the latent representations z . Then, the HMC is applied to sample the parameters of the last layer θ_{LL} .

Algorithm 1 Last Layer Hamiltonian Monte Carlo

Parameters – θ : Network parameters, B : Burn-in period, E : Number of epochs, C : Number of chains, S : Number of HMC samples, P : Parameter storage matrix

- 1: Randomly initialize network parameters θ
 - 2: **Phase 1 – Optimization-based pre-training:**
 - 3: **for** $e \leftarrow 1, \dots, E$ **do**
 - 4: Update $\theta^{(e)}$ using a stochastic optimizer (e.g., SGD/ADAM)
 - 5: **end for**
 - 6: Remove the last layer (θ_{LL}) and process the raw input data produce the latent representations \mathbf{Z} for the dataset
 - 7: **Phase 2 – HMC Sampling for θ_{LL} :**
 - 8: Initialize the last layer’s parameters θ_{LL}
 - 9: **for** $c \leftarrow 1, \dots, C$ **do**
 - 10: **for** $s \leftarrow 1, \dots, S$ **do**
 - 11: Perform HMC to generate a new sample θ'_{LL}
 - 12: **if** $s > B$ **then** ▷ After burn-in period
 - 13: Add θ'_{LL} to $P[c, s]$
 - 14: **end if**
 - 15: **end for**
 - 16: **end for**
-

(2020) Rong et al. (2020) extracted and predicted the optical flow for the exterior cameras. Vellenga et al. (2024) Vellenga et al. (2024b) fine-tuned video masked auto-encoders and attention fusion to improve DAR and DIR performance. Although these DAR and DIR approaches have incrementally improved performance, they have not considered the uncertainty-based OOD detection, which is a critical aspect for safe driving automation.

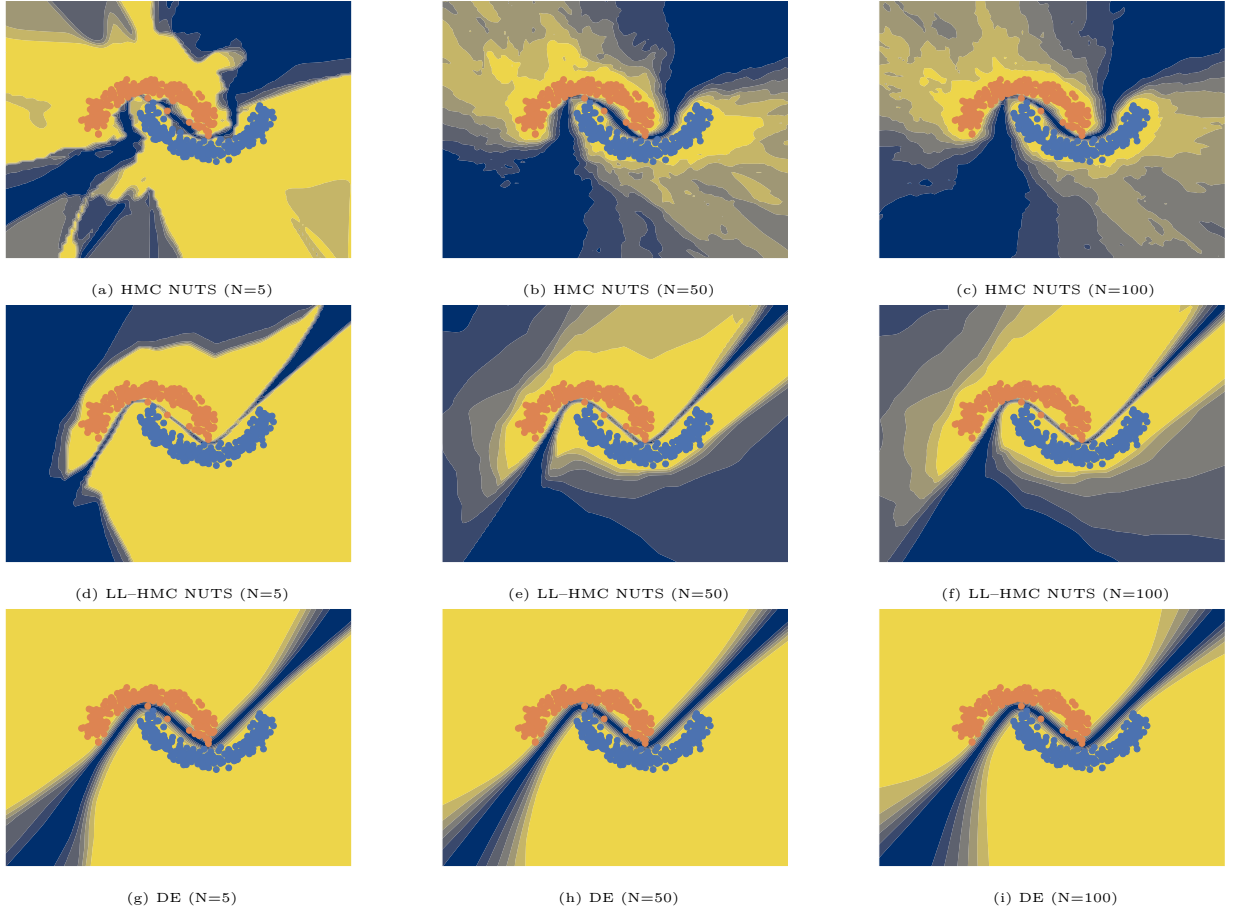


Figure 3: Toy two moons classification example results. First row consists of full HMC with 5, 50, and 100 samples, the second row shows the LL-HMC results, and the third row shows the results for a deep ensemble. The yellow area denotes certain predictions, whereas the dark blue area indicates uncertain predictions. The certain (yellow) vs uncertain (dark blue) color map is normalized.

3 Last layer Hamiltonian Monte Carlo

Given that HMC sampling scales poorly to larger DNNs and bigger datasets, LL-HMC restricts the HMC sampling procedure to the final layer of a DNN. This simplification reduces the computational burden, but introduces a dependency on the fixed trained latent representations. We divide the LL-HMC approach into two phases: optimization-based training and HMC-sampling for the last layer θ_{LL} (see Algorithm 1 and Figure 2). Phase 1 concerns regular training or fine-tuning of the DNN using a standard gradient-based optimizer (e.g., stochastic gradient descent [SGD] or ADAM) to update all layers of a network θ . Once the training (or fine-tuning) is complete, the last layer θ_{LL} is removed, and the latent representations \mathbf{z} are extracted from the penultimate layer for the training, test, and OOD datasets. Before starting the HMC sampling, we randomly initialize the parameter values of θ_{LL} . Then, for each chain C , HMC sampling is performed for θ_{LL} to estimate the posterior distribution given the latent representations \mathbf{z} instead of the original raw data. HMC treats the model parameters as positions in a dynamical system to facilitate exploration of the posterior. The HMC algorithm uses the leapfrog integrator to propose new parameter values θ'_{LL} by simulating the dynamics of the Hamiltonian system. The NUTS sampler (Hoffman et al., 2014) dynamically adjusts the number of leapfrog steps in HMC to avoid inefficient exploration of the parameter space. The acceptance ratio between the current state $(\theta_{LL}, \mathbf{p})$ and the proposed state $(\theta'_{LL}, \mathbf{p}')$ guides the decision to accept or reject the proposed parameters.

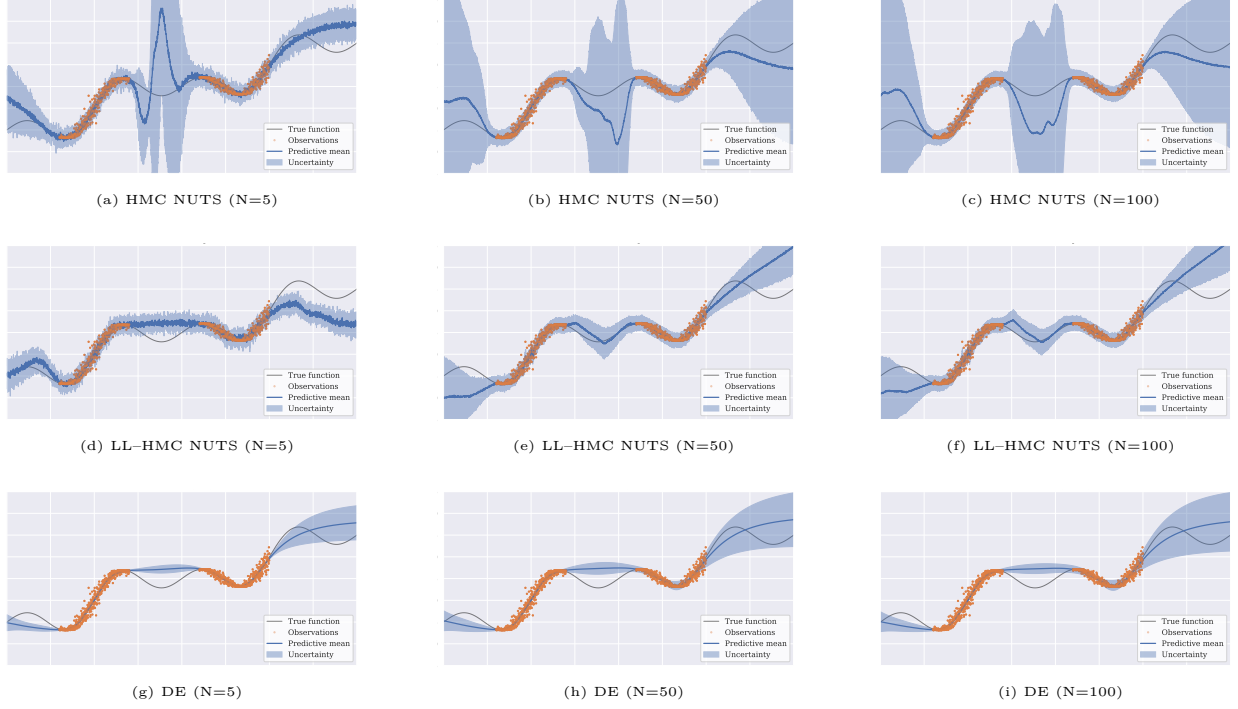


Figure 4: Toy Regression Example results. First row consists of full HMC with 5, 50, and 100 samples, the second row shows the LL-HMC results, and the third row shows the results for a deep ensemble. The y-axis is the target variable, the x-axis the observations. The gray line is the original function, the orange dots represent the noisy observations, the blue line the mean prediction, and the light blue area the uncertainty estimation.

3.1 Toy-examples

We visualize the uncertainty estimation capabilities of LL-HMC using a classification and a regression toy example. Specifically, we compare LL-HMC to HMC sampling on the entire network and a DE that uses a similar number of samples. We use the two moons dataset (Pedregosa et al., 2011) with a multi-layer perceptron with two hidden layers of 20 units, following the implementation from van Van Amersfoort et al. (2020). Figure 3 shows where the different methods are certain (yellow) and uncertain (dark blue) for the two moons dataset. With more samples, full HMC gradually becomes more uncertain in areas for which no data has been observed. LL-HMC becomes more uncertain in unobserved areas as the number of samples increases from 5 to 50. However, the uncertainty estimations do not improve further with additional samples, indicating the limitations of the LL-HMC approach. In congruence with Van Amersfoort et al. (2020), we observe that the DE mostly remains uncertain along the decision boundary and only improves slightly with more ensemble members.

To evaluate the uncertainty estimations for a regression toy example, we use the implementation of Lippe (2022) to generate noisy observations from a sinusoidal function. The underlying architecture is an MLP with five hidden layers and 50 hidden units for all methods. Figure 4 shows the uncertainty estimation results for the toy regression example. When performing HMC on the entire DNN, we observe higher uncertainty in regions without observations. For both the LL-HMC and the deep ensemble, the uncertainty between the two observation areas remains relatively stable, further highlighting the advantage of full-network HMC in capturing the uncertainty.

4 Experimental setup

4.1 Datasets

For the DAR task, we use the AssIstive Driving pErception (AIDE) dataset (Yang et al., 2023) that consists of 2898 short videos recorded in China, with the following labels: 185 *backward moving*, 1522 *forward moving*, 138 *lane changing*, 727 *parking*, and 326 *turning*. Additionally, we use annotations from the ROad event Awareness Dataset (ROAD) (Singh et al., 2022), which extend a subset of 22 videos (122,000 frames) of the Oxford RobotCar Dataset (Maddern et al., 2017) with ego-vehicle and road user driving action labels. Since the ROAD data was collected with manual driving, the vehicle action labels reflect human driving maneuvers (Maddern et al., 2017). To capture temporal patterns, we transform the frame-level annotations into video-level labels by selecting only driving actions with at least 8 consecutive frames. This threshold ensures that each clip provides sufficient temporal context for distinguishing maneuvers while reducing ambiguous or noisy labels. As a result, the offline ROAD DAR dataset consists of 75 *stopping*, 162 *move forward*, 31 *turn right*, 41 *turn left*, 12 *move right*, 12 *move left* and 8 *overtake* maneuvers.

For DIR, we use the open-source Brain4Cars (B4C) dataset (Jain et al., 2015) collected in the United States. The B4C dataset consists of 124 *left lane changes*, 123 *right lane changes*, 58 *left turns*, 55 *right turns*, and 234 *driving straight* maneuvers. We retain the natural class imbalance present in all datasets to reflect the real-world distribution of driving behaviors. For all datasets, we use the original train-test splits. For the ROAD and B4C datasets, we use the first fold from the provided splits.

4.2 Metrics

Performance, and uncertainty. We report standard metrics (accuracy \uparrow , F1-score \uparrow) to measure the in-distribution performance. To understand the differences between the PDL methods, we use two times the standard error of the mean (2SEM, Barde & Barde 2012, Equation 1) instead of the standard deviation (the variability across random seeds). 2SEM roughly corresponds to the 95% confidence interval of the mean performance of each PDL method. To estimate uncertainty, we use predictive entropy (Smith & Gal, 2018) (Equation 2), which is maximized when the probabilities are uniformly distributed among all classes. The more confident the model is in its predictions for a particular class, the lower the predictive entropy will be, indicating less uncertainty.

$$2SEM = 2\frac{\sigma}{\sqrt{n}}, \quad (1)$$

where:

σ =standard deviation, and
 n =number of observations.

$$H[P(y|x)] = - \sum_{y \in \mathcal{Y}} P(y|x) \log P(y|x), \quad (2)$$

where:

$H[P(y|x)]$ =the entropy of the predictive distribution,
 $P(y|x)$ =conditional probability distribution, over some discrete set of outcomes \mathcal{Y} , and
 \mathcal{Y} =set of N stochastic predictions.

Calibration. To measure the alignment between the prediction confidence and the performance, we use the adaptive calibration error (ACE \downarrow , Nixon et al. 2019, Equation 3) with 10 bins. ACE partitions predictions into adaptively-sized bins, comparing the average predicted probability in each bin to the corresponding fraction of correct predictions. Overconfidence occurs when predicted confidence exceeds accuracy; conservativeness

occurs when confidence falls short of accuracy. To assess the quality of the uncertainty estimates relative to model performance, we use the relative Area Under the Lifted Curve (rAULC \uparrow , Postels et al. 2022, Equation 4). The rAULC evaluates how well uncertainty scores are calibrated. Ideally, confident and correct predictions should correspond to low uncertainty, while incorrect or low-confidence predictions should yield high uncertainty.

$$ACE = \frac{1}{KR} \sum_{k=1}^K \sum_{r=1}^R |acc(r, k) - conf(r, k)|, \quad (3)$$

where:

k =class label,
 r =adaptive range for class label,
 $acc(r, k)$ =accuracy within a bin, and
 $conf(r, k)$ =predicted confidence within a bin.

$$rAULC = -1 + \sum_{i=1}^S \frac{s \cdot A(q_i)}{R(q_i)}, \quad (4)$$

where:

q_i =uncertainty quantiles $i \in [1, \dots, S]$,
 s =quantile step width based on the number of predictions in the test dataset ($1/N$),
 $A(q_i)$ =accuracy of samples with uncertainty below quantile q_i ,
 $R(q_i)$ =expected accuracy for random guessing at quantile q_i ,
 S =total number of quantiles.

MCMC diagnostics. We evaluate the quality of posterior samples using the Effective Sample Size (ESS, Geyer 1992, Equation 5). A higher ESS implies better exploration of the posterior distribution. For LL-HMC with multiple chains, we use Gelman’s \hat{R} statistic (Gelman & Rubin, 1992) to assess convergence (Equation 6). \hat{R} compares the variance between chains to the variance within each chain. Values close to 1 suggest that the chains are exploring the same distribution (Izmailov et al., 2021).

$$ESS(N) = N / \left(1 + 2 \times \sum_{k=1}^{N-1} \left(1 - \frac{k}{N} \right) \times R_k \right), \quad (5)$$

where:

N =total number of samples, and
 R_k =the auto-correlation at lag k .

$$\hat{R} = \frac{E[\text{Var}[X|\text{chain}]] + \text{Var}[E[X|\text{chain}]]}{E[\text{Var}[X|\text{chain}]]}, \quad (6)$$

where:

$E[\text{Var}[X|\text{chain}]]$ =the expected value of the variance of X given the chain, and
 $\text{Var}[E[X|\text{chain}]]$ =the variance of the expected value of X given the chain.

OOD detection. To determine whether OOD instances yield high uncertainty, we compute the Area Under the Receiver Operating Characteristic (ROC, \uparrow) and Precision-Recall (PR, \uparrow) curves (Malinin & Gales, 2018; Durasov et al., 2024). Furthermore, we report the False Positive Rate at 95% Recall (FPR95, \downarrow). FPR95 measures the proportion of OOD instances that are incorrectly classified as in-distribution when the model correctly identifies 95% of in-distribution samples.

4.3 Underlying model architecture

Given the relatively small size of the DAR and DIR datasets, we use a Kinetics-400 (Kay et al., 2017) self-supervised pre-trained Video Masked Autoencoder (VMAE, Tong et al. 2022). As a backbone, the VMAE uses a Vision Transformer (ViT) Base architecture (Arnab et al., 2021) that consists of about 94 million parameters. The ViT-Base expects videos of 16 frames, has a depth of 12 blocks and a hidden latent dimension of 768. For the datasets with multiple video streams, we combine the latent modality representations via attentional feature fusion (Dai et al., 2021).

4.4 Implementation details

We fine-tune a separate ViT-Base model for 20 epochs per dataset using the AdamW optimizer (Loshchilov & Hutter, 2018) with a weight decay of 0.05. We apply early stopping with a patience of 5 epochs and set the learning rate to $5e-5$. We use an Ubuntu 20.04 server with two 16GB NVIDIA Tesla T4 GPUs. To simulate a larger batch size of 8, we use the gradient accumulation module from the Accelerate library (Gugger et al., 2022).

The LL-HMC experiments are run on a separate Ubuntu 20.04 server (CPU-only, 60GB RAM) using the NUTS sampler from Pyro (Bingham et al., 2018). We perform a grid search for 5 random seeds for different prior standard deviation (0.01, 0.1, 1, 2.5, 5, 10), number of burn-in samples (10, 25, 50, 100, 200), target acceptance probabilities (0.6, 0.7, 0.8), multiple chains (1, 2) and numbers of collected samples (2, 5, 10, 15, 20, 25, 30, 35, 40, 45, 50) for the classification layer θ_{LL} . When we use more than a single chain, we divide the number of collected samples evenly over the chains. For the LL-HMC with multiple starting positions (latent representations from different independently fine-tuned models), we use the top-performing ensemble models to produce the latent representations.

For the remaining last layer PDL (LL-PDL) methods, we also perform a grid search for the same random seeds to evaluate the number of samples/predictors/ensemble members (5, 10, 15, 20, 25, 30, 35, 40, 45, 50), batch size (16, 32, 64), learning rate ($1e-2$, $1e-3$, $1e-4$) for different numbers of epochs (5, 10, 15, 20, 25). For VBLL (Harrison et al., 2024), which does not produce multiple predictions, we evaluate modifying the KL regularization (1, 5, 10).

4.5 Experiments

4.5.1 Video-based DAR and DIR performance

To compare LL-HMC to other PDL methods, we use the fine-tuned ViT-Base models as a regular baseline. The baseline models also produce the latent representations on which the other LL-PDL methods rely. Additionally, we also evaluate an ensemble of 5 independently fine-tuned ViT-Base models. For the LL-PDL methods, we include the following approaches that do not require any form of post-hoc calibration: SE (Valdenegro-Toro, 2023), DDU (Mukhoti et al., 2023), BBB (Blundell et al., 2015), PE (Laurent et al., 2023), and VBLL (Harrison et al., 2024).

4.5.2 Uncertainty-based out-of-distribution detection

OOD detection aims to identify inputs that do not belong to the distribution of the training data (Yang et al., 2024). To construct realistic OOD instances for DAR and DIR, we remove the most and least prevalent classes from each dataset to simulate OOD instances for common or rare maneuvers. The removed classes from both the train and test datasets serve as the unseen OOD instances. We fine-tune a ViT-Base model on each reduced training set to obtain latent representations to use for the PDL methods. For the ROAD

Table 1: Average performance and two standard errors of the mean of the top-performing hyperparameter configurations per random seed for the AIDE, B4C and ROAD datasets. Each PDL method, except for the deep ensemble, uses the latent representations produced by the *Regular* model. Acc=Accuracy, ACE=Adaptive Calibration Error with 10 bins, rAULC=relative Area under the lifted curve.

	AIDE (Yang et al., 2023)				B4C (Jain et al., 2015)				ROAD (Singh et al., 2022)			
	Acc (↑)	F1 (↑)	ACE (↓)	rAULC (↑)	Acc (↑)	F1 (↑)	ACE (↓)	rAULC (↑)	Acc (↑)	F1 (↑)	ACE (↓)	rAULC (↑)
Regular	87.19	81.88	0.027	0.77	92.31	93.71	0.050	0.53	71.64	45.36	0.063	0.61
DE (N=5)	89.66	82.24	0.019	0.80	90.88	91.49	0.059	0.73	74.24	44.57	0.066	0.70
DDU	57.31	19.12	0.088	0.85	76.07	74.72	0.124	0.61	59.70	23.85	0.138	0.42
BBB-LL	88.67±0.36	83.13±0.26	0.032±0.005	0.73±0.02	93.16±0.94	94.28±0.87	0.025±0.007	0.65±0.08	71.64±3.13	56.14±4.37	0.068±0.003	0.50±0.13
PE-LL	88.64±0.32	83.37±0.02	0.030±0.003	0.74±0.01	94.02±2.24	95.02±0.02	0.022±0.005	0.67±0.03	68.66±2.11	59.28±1.38	0.077±0.008	0.36±0.09
SE	88.31±0.19	82.69±0.21	0.029±0.000	0.75±0.01	93.16±0.18	94.38±0.04	0.023±0.001	0.72±0.00	68.06±2.23	45.63±2.45	0.065±0.002	0.57±0.01
VBLL	88.67±0.36	83.13±0.26	0.032±0.005	0.73±0.02	92.14±1.26	93.47±1.13	0.116±0.038	0.55±0.10	72.54±2.60	47.25±2.08	0.084±0.004	0.48±0.05
LL-HMC	89.00±0.16	83.87±0.08	0.029±0.002	0.68±0.06	94.02±0.42	95.00±0.29	0.027±0.007	0.66±0.10	70.15±5.05	54.18±4.43	0.073±0.014	0.41±0.12

Table 2: Average grid search results and two standard errors of the mean for the best average hyperparameter configuration across five random seeds.

	AIDE (Yang et al., 2023)				B4C (Jain et al., 2015)				ROAD (Singh et al., 2022)			
	Acc (↑)	F1 (↑)	ACE (↓)	rAULC (↑)	Acc (↑)	F1 (↑)	ACE (↓)	rAULC (↑)	Acc (↑)	F1 (↑)	ACE (↓)	rAULC (↑)
BBB-LL	88.47±0.41	82.49±0.41	0.030±0.001	0.70±0.05	90.09±1.16	91.26±1.70	0.028±0.005	0.80±0.02	63.58±5.05	34.51±1.72	0.077±0.007	0.62±0.04
PE-LL	87.85±0.63	80.61±2.12	0.034±0.004	0.79±0.02	91.97±0.42	91.99±0.45	0.021±0.002	0.84±0.01	65.37±1.12	29.72±1.12	0.092±0.002	0.67±0.02
SE	88.11±0.13	81.61±0.11	0.028±0.001	0.77±0.01	92.14±0.34	92.21±0.26	0.022±0.002	0.82±0.00	65.97±0.60	29.45±0.32	0.103±0.002	0.67±0.02
VBLL	87.95±0.17	78.62±3.17	0.034±0.003	0.78±0.02	86.32±3.01	84.92±3.17	0.081±0.007	0.80±0.07	66.27±1.52	31.29±1.71	0.108±0.005	0.63±0.03
LL-HMC	88.44±0.22	82.69±0.26	0.028±0.000	0.76±0.01	90.26±1.39	90.17±2.46	0.027±0.004	0.85±0.03	61.79±4.07	32.03±4.00	0.083±0.010	0.63±0.15

dataset, removing the most occurring maneuver would leave a subset of fewer than 200 videos. Therefore, for the ROAD dataset, we only apply the OOD-min setting, where we remove the maneuvers for which we have less than 20 videos (*Move Right*, *Move Left*, and *Overtake*).

5 Results

To avoid reliance on a single random initialization (Bouthillier et al., 2019), we examine classification and OOD detection performance differences across multiple random seeds. For both the in-distribution and OOD experiments, we first analyze the grid search results across five random seeds. We present the top performance averaged across random seeds to illustrate classification and OOD detection results for a single grid search. Next, we report the performance of the best average hyperparameter configuration across the random seeds. To better understand the differences between the included LL-PDL methods, as well as the effects of additional predictions or sampled last-layer parameters, we use the best average hyperparameter configuration and conduct further evaluations with more random seeds. For LL-HMC, we also analyze the influence of the prior, additional chains, additional starting positions, parameter trajectories, and MCMC diagnostics.

5.1 In-distribution action and intention recognition performance

Grid search results. Table 1 reports the average performance of the top hyperparameter configuration per random seed. Table 2 shows the performance of the single hyperparameter configuration that achieved the best average across the random seeds. The regular DNN serves as the baseline, and the DE and DDU were only evaluated once per dataset. For the DDU, the lower performance is most likely due to the absence of spectral normalization. The variability in DE performance may be attributed to the small ensemble size (N=5), which limits its robustness. Given the computational cost of adding more members, DE may not be practical for resource-constrained operating environments.

The top-performing LL-HMC configurations in Table 1 consistently achieve performance comparable to the best-performing PDL methods. From a confidence-performance calibration perspective (ACE), the BBB-LL, PE-LL, SE and LL-HMC yield a lower ACE for the B4C and ROAD datasets compared to the regular model, but not for the AIDE dataset. Additionally, no single method optimally balances both classification performance and calibration across all datasets. The regular softmax-based model is better calibrated than the LL-HMC approach, except for the B4C dataset. Additionally, we do not observe that the higher classification

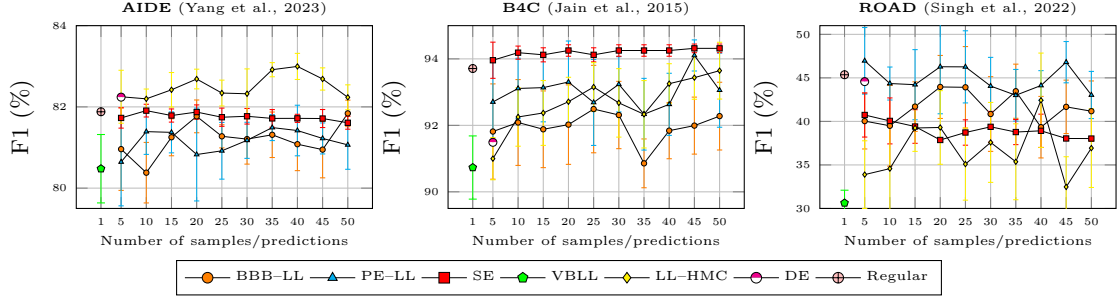


Figure 5: Influence of the number of samples or predictions for independent random seeds for the average best-performing hyperparameter configurations of the included PDL methods. The regular model (single prediction), DE (N=5), and VBLL (single prediction) are only included once in each figure. For each number of samples, the whiskers indicate two standard errors of the mean for 10 runs for different random seeds for every number of samples to avoid dependencies.

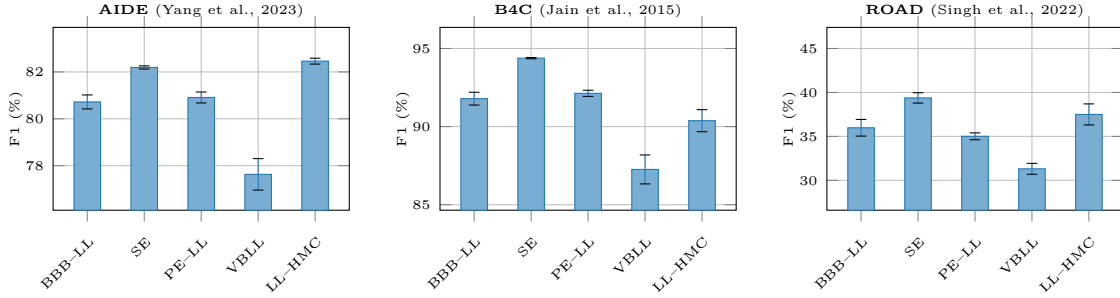


Figure 6: Average F1-scores and two standard errors of the mean across the included LL-PDL methods for the best performing grid search hyperparameter configurations across 100 random seeds.

performance of LL-HMC in Table 1 also results in an improved rAULC (the ability to distinguish between correctly and incorrectly predicted in-distribution instances based on the uncertainty estimations).

While Table 1 presents the potential top-performance we could observe when we would perform a single grid search, Table 2 reveals that using the average hyperparameter configuration across seeds leads to significantly lower average in-distribution classification performance. More specifically, the F1-scores dropped on average with 2.1, 4.3 and 21.1 for the AIDE, B4C and ROAD datasets respectively. The larger performance drop on the ROAD dataset suggests that LL-PDL methods may be more sensitive to observation noise and initialization instability, particularly in smaller or noisier datasets.

Influence of additional predictions or samples. For the ViT-Base architecture, processing a single 16-frame video requires approximately 361×10^9 floating point operations (FLOPs). The majority of the FLOPs are required to produce the latent representation on which the LL-PDL methods rely. Every additional last layer sample or prediction requires 7.68 or 9.22×10^3 FLOPs for a classifier with 5 or 6 classes respectively. Considering the 361×10^9 FLOPs that are required to produce the latent representation \mathbf{z} , the computational impact of the additional predictions are relatively negligible. To examine the influence of additional predictions or sampled last layers, we evaluated the top configurations from Table 2 for 10 different random seeds for each number of samples. Figure 5 illustrates the average performance and two standard errors of the mean for each number of samples. For the LL-PDL methods, no clear trend indicates that additional samples (or predictions) consistently improves the performance. Additionally, we observe that for each dataset another LL-PDL method performs best on average.

Comparing the best hyperparameter configurations. To evaluate whether any of the included LL-PDL methods consistently outperforms others, we tested the average best performing hyperparameter

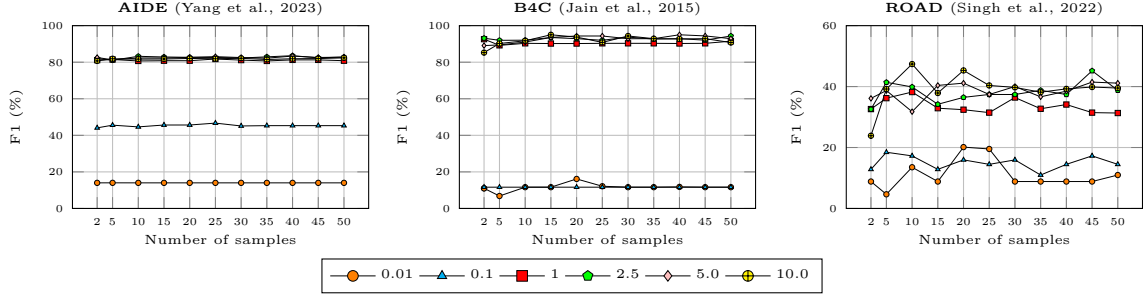


Figure 7: Effect of different prior standard deviation values and the number of samples on the LL-HMC in-distribution performance with a target acceptance of 0.7 and 100 burn-in samples for a single random seed.

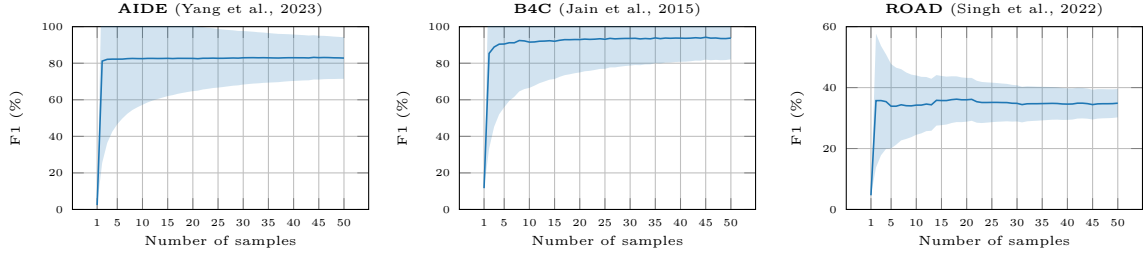


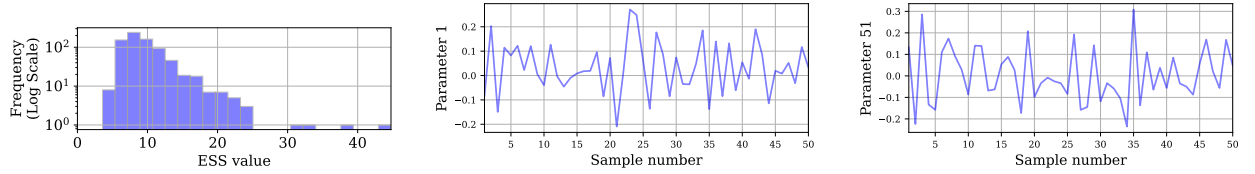
Figure 8: Effects of additional dependent samples from the same chain for the top-performing LL-HMC configuration across 100 random seeds. The light blue area illustrates the standard deviation of the cumulative F1-score for the additional samples.

configuration from Table 2 across 100 different random seeds. Figure 6 illustrates the average DAR and DIR classification performance for each dataset and method. Consistent with the results in Figure 5, no method consistently achieves the best average performance across the datasets. VBLL exhibits higher standard errors across datasets, suggesting greater sensitivity to random seed variations. As also observed in Table 2, the performance degradation from top-performing configurations is more pronounced in the smaller ROAD dataset.

Prior scale influence. To investigate the impact of prior scale on LL-HMC, Figure 7 shows the relationship between F1-score and the number of HMC samples, for multiple prior standard deviations. Because the last layer is randomly initialized (cold start) with uninformative priors, smaller prior scales (i.e., stricter priors) tend to degrade performance. For the AIDE and B4C datasets, performance plateaus after 5–10 samples, suggesting that further samples yield negligible performance gains. This implies that LL-HMC achieves stable predictive performance with relatively few samples, which is beneficial for computational efficiency. The ROAD dataset exhibits greater sensitivity to prior scale and the number of samples, with more variation in F1-score across configurations.

Influence of additional dependent LL-HMC samples. To examine how additional samples from the same LL-HMC chain affect DAR and DIR performance, Figure 8 presents the average F1 score and the standard deviation as more samples are cumulatively drawn across 100 random seeds. The results show that standard deviation decreases with more samples, but performance converges quickly. This suggests that beyond a small number of posterior samples, further samples from the LL-HMC chain yield diminishing returns in classification performance.

Effective sample size and parameter trajectories. Figure 9 includes a histogram of effective sample size (ESS) values across parameters (x-axis: ESS; y-axis: number of parameters), along with two example parameter trajectories. Consistent with findings in Vellenga et al. (2024a), LL-HMC yields a low ESS for



ESS per last layer parameter for the AIDE dataset with a single chain for 50 samples.

Value for the first weight parameter of the last layer for each sample.

Value for the fifty-first weight parameter of the last layer for each sample.

Figure 9: Visualization of the ESS and the parameter values for 50 samples for LL-HMC for the AIDE dataset with a single chain, target acceptance of 0.7, prior standard deviation of 1, and 100 burn in samples.

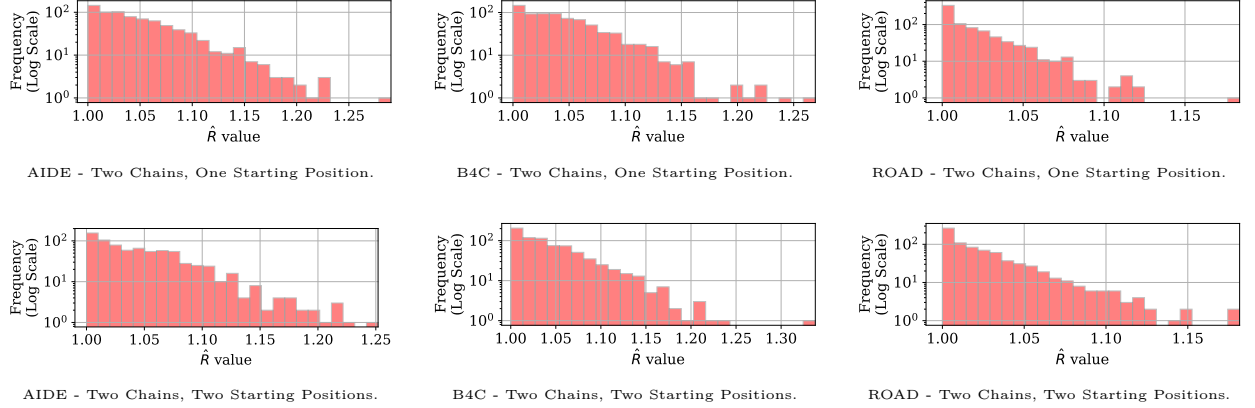


Figure 10: Log-scale histograms of the \hat{R} values for two chains for single starting position (top) or two starting positions (bottom), for 100 burn-in samples, target acceptance of 0.7, 50 samples and a prior scale of 1.

Table 3: Average top-performance and two standard errors of the mean across five random seeds for LL-HMC with multiple starting positions or chains. S=Starting Positions, C=Chains.

		AIDE (Yang et al., 2023)				B4C (Jain et al., 2015)				ROAD (Singh et al., 2022)				
		Acc (†)	F1 (†)	ACE (↓)	rAULC (†)	Acc (†)	F1 (†)	ACE (↓)	rAULC (†)	Acc (†)	F1 (†)	ACE (↓)	rAULC (†)	
LL-HMC	S=1	C=1	89.00±0.16	83.87±0.08	0.029±0.002	0.68±0.06	93.73±0.42	94.78±0.29	0.027±0.007	0.66±0.10	70.15±5.05	54.18±4.43	0.073±0.014	0.41±0.12
		C=2	88.34±0.73	82.98±0.25	0.045±0.017	0.66±0.06	93.59±0.42	94.74±0.32	0.032±0.011	0.61±0.03	68.16±5.12	53.51±0.93	0.077±0.017	0.16±0.09
	S=2	C=1	89.00±0.17	83.66±0.32	0.029±0.002	0.70±0.03	94.02±0.11	95.00±0.07	0.023±0.001	0.70±0.02	69.16±4.66	52.67±2.45	0.072±0.015	0.57±0.07
		C=2	88.15±0.46	82.56±0.60	0.042±0.007	0.60±0.03	93.59±0.42	94.72±0.30	0.047±0.019	0.52±0.07	70.90±4.76	53.79±3.05	0.081±0.017	0.27±0.19

most parameters, indicating effective sampling only for a small subset. The example parameter trajectories show no discernible trend or drift and fluctuate around zero, suggesting limited exploration.

Multiple chains and starting positions. Table 3 shows the average top-performing configurations across five random seeds for multiple starting (S) positions and multiple chains (C). The results show that increasing the number of chains or adding an additional starting position does not consistently lead to improved performance. When using multiple chains, it is also important to assess whether the chains have explored distinct regions of the posterior and converged to the target distribution. Figure 10 shows the \hat{R} values for the scenarios with multiple chains for both single and multiple starting positions. For all datasets, the \hat{R} values are close to 1 and mostly below 1.1. This indicates that the chains have likely converged to the target distribution but also potentially sample from the same region (Izmailov et al., 2021).

5.2 Uncertainty-based out-of-distribution detection performance

Grid search results. Table 4 reports the average OOD detection performance for the top-performing hyperparameter configurations per random seed. Table 5 shows the results of the single hyperparameter configuration that achieved the best average performance across the random seeds. For every OOD scenario,

Table 4: Average uncertainty-based OOD detection performance and two standard errors of the mean of the top-performing hyperparameter configurations per random seed. ROC-AUC=Receiver Operating Characteristic - Area Under the Curve, PR=Precision-Recall - Area Under the Curve.

	AIDE (Yang et al., 2023)						B4C (Jain et al., 2015)						ROAD (Singh et al., 2022)		
	ROC-AUC (\uparrow)	OOD min PR-AUC (\uparrow)	FPR95 (\downarrow)	ROC-AUC (\uparrow)	OOD max PR-AUC (\uparrow)	FPR95 (\downarrow)	ROC-AUC (\uparrow)	OOD min PR-AUC (\uparrow)	FPR95 (\downarrow)	ROC-AUC (\uparrow)	OOD max PR-AUC (\uparrow)	FPR95 (\downarrow)	ROC-AUC (\uparrow)	OOD min PR-AUC (\uparrow)	FPR95 (\downarrow)
Regular	0.55	0.19	0.91	0.82	0.94	0.41	0.51	0.37	0.90	0.64	0.82	0.84	0.19	0.25	1.00
DE (N=5)	0.69	0.28	0.85	0.84	0.94	0.35	0.52	0.39	0.90	0.79	0.90	0.45	0.55	0.41	0.88
DDU	0.73	0.31	0.49	0.80	0.90	0.45	0.63	0.44	0.87	0.48	0.75	0.96	0.63	0.44	0.87
BBB-LL	0.95 \pm 0.02	0.72 \pm 0.08	0.10 \pm 0.05	0.96 \pm 0.01	0.99 \pm 0.01	0.22 \pm 0.06	0.84 \pm 0.03	0.70 \pm 0.04	0.48 \pm 0.21	0.80 \pm 0.02	0.92 \pm 0.01	0.69 \pm 0.10	0.60 \pm 0.10	0.49 \pm 0.13	0.85 \pm 0.06
PE-LL	0.55 \pm 0.01	0.52 \pm 0.01	0.83 \pm 0.01	0.56 \pm 0.01	0.53 \pm 0.01	0.72 \pm 0.02	0.52 \pm 0.01	0.52 \pm 0.01	0.91 \pm 0.01	0.53 \pm 0.01	0.53 \pm 0.00	0.94 \pm 0.02	0.53 \pm 0.01	0.52 \pm 0.01	0.92 \pm 0.01
SE	0.59 \pm 0.01	0.21 \pm 0.01	0.89 \pm 0.01	0.88 \pm 0.01	0.96 \pm 0.01	0.41 \pm 0.01	0.72 \pm 0.02	0.54 \pm 0.01	0.50 \pm 0.02	0.71 \pm 0.01	0.88 \pm 0.01	0.79 \pm 0.01	0.45 \pm 0.05	0.33 \pm 0.02	0.86 \pm 0.10
VBLL	0.66 \pm 0.04	0.25 \pm 0.03	0.79 \pm 0.08	0.89 \pm 0.01	0.97 \pm 0.01	0.42 \pm 0.04	0.82 \pm 0.05	0.64 \pm 0.07	0.41 \pm 0.09	0.65 \pm 0.02	0.84 \pm 0.02	0.88 \pm 0.06	0.57 \pm 0.09	0.44 \pm 0.11	0.80 \pm 0.05
LL-HMC	0.91 \pm 0.03	0.58 \pm 0.10	0.18 \pm 0.05	0.95 \pm 0.01	0.99 \pm 0.01	0.14 \pm 0.01	0.85 \pm 0.04	0.73 \pm 0.05	0.36 \pm 0.08	0.91 \pm 0.01	0.97 \pm 0.01	0.39 \pm 0.05	0.87 \pm 0.01	0.72 \pm 0.01	0.31 \pm 0.04

Table 5: Average uncertainty-based OOD detection grid search results and two standard errors of the mean for the best average hyperparameter configuration across five random seeds.

	AIDE (Yang et al., 2023)						B4C (Jain et al., 2015)						ROAD (Singh et al., 2022)		
	ROC-AUC (\uparrow)	OOD min PR-AUC (\uparrow)	FPR95 (\downarrow)	ROC-AUC (\uparrow)	OOD max PR-AUC (\uparrow)	FPR95 (\downarrow)	ROC-AUC (\uparrow)	OOD min PR-AUC (\uparrow)	FPR95 (\downarrow)	ROC-AUC (\uparrow)	OOD max PR-AUC (\uparrow)	FPR95 (\downarrow)	ROC-AUC (\uparrow)	OOD min PR-AUC (\uparrow)	FPR95 (\downarrow)
BBB-LL	0.55 \pm 0.11	0.20 \pm 0.04	0.84 \pm 0.15	0.80 \pm 0.06	0.93 \pm 0.02	0.58 \pm 0.20	0.32 \pm 0.05	0.30 \pm 0.02	0.99 \pm 0.03	0.50 \pm 0.11	0.76 \pm 0.07	0.92 \pm 0.04	0.29 \pm 0.06	0.28 \pm 0.02	0.97 \pm 0.04
PE-LL	0.50 \pm 0.00	0.50 \pm 0.00	0.95 \pm 0.01	0.51 \pm 0.00	0.51 \pm 0.00	0.93 \pm 0.01	0.51 \pm 0.00	0.51 \pm 0.00	0.95 \pm 0.01	0.52 \pm 0.01	0.51 \pm 0.01	0.94 \pm 0.01	0.51 \pm 0.00	0.51 \pm 0.00	0.95 \pm 0.00
SE	0.51 \pm 0.01	0.17 \pm 0.00	0.86 \pm 0.02	0.81 \pm 0.00	0.93 \pm 0.00	0.41 \pm 0.01	0.29 \pm 0.00	0.29 \pm 0.00	1.00 \pm 0.00	0.32 \pm 0.02	0.69 \pm 0.01	0.99 \pm 0.01	0.17 \pm 0.01	0.24 \pm 0.00	1.00 \pm 0.00
VBLL	0.44 \pm 0.02	0.14 \pm 0.01	0.96 \pm 0.02	0.54 \pm 0.14	0.84 \pm 0.07	0.88 \pm 0.13	0.49 \pm 0.10	0.36 \pm 0.07	0.90 \pm 0.12	0.48 \pm 0.03	0.42 \pm 0.04	0.96 \pm 0.02	0.16 \pm 0.03	0.24 \pm 0.01	0.99 \pm 0.01
LL-HMC	0.53 \pm 0.02	0.18 \pm 0.01	0.87 \pm 0.05	0.82 \pm 0.06	0.94 \pm 0.02	0.48 \pm 0.20	0.57 \pm 0.06	0.42 \pm 0.04	0.78 \pm 0.10	0.57 \pm 0.06	0.74 \pm 0.02	0.78 \pm 0.10	0.28 \pm 0.08	0.27 \pm 0.02	0.97 \pm 0.03

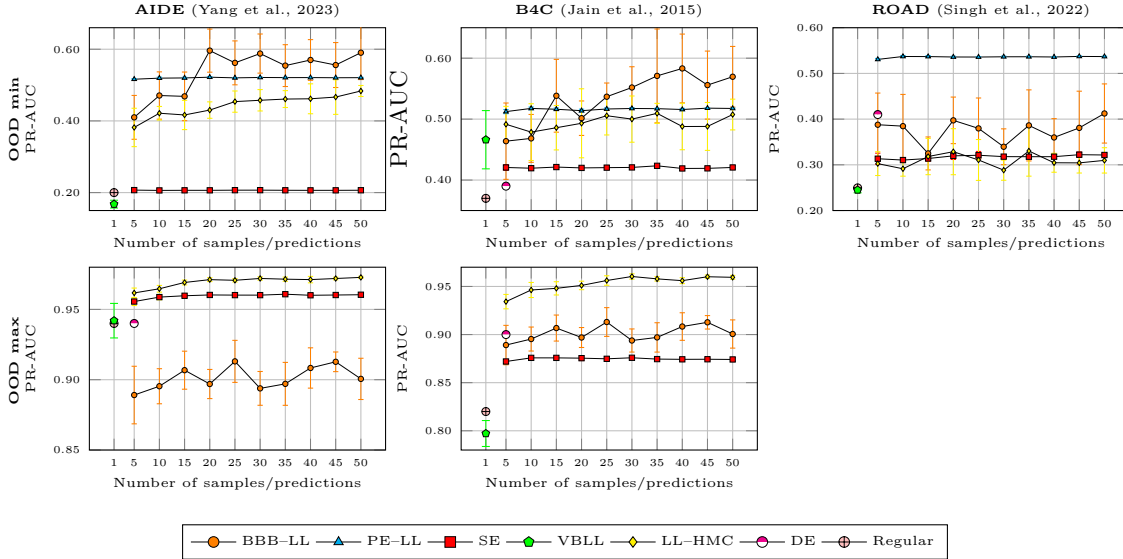


Figure 11: Influence of the number of samples or predictions on the OOD detection across 10 different random seeds for the average best-performing hyperparameter configuration of the included PDL methods. For each number of samples, the whiskers indicate two standard errors of the mean. Markers without visible whiskers indicate small standard errors. For the OOD max figures, the PE-LL is filtered out due to lower OOD performance.

at least one PDL method outperforms the regular softmax baseline. Table 4 shows that the top-performing LL-HMC configuration produces the top or the best uncertainty-based OOD detection results. The other PDL methods also exhibit comparable, and at times superior, performance. However, as observed for in-distribution classification results, Table 5 highlights that the grid searched hyperparameter configurations are in most scenarios not robust to different random seeds and often result in substantial performance degradation. Only the AIDE OOD max scenario (with the most OOD instances) shows comparable performance to the top-performing configurations.

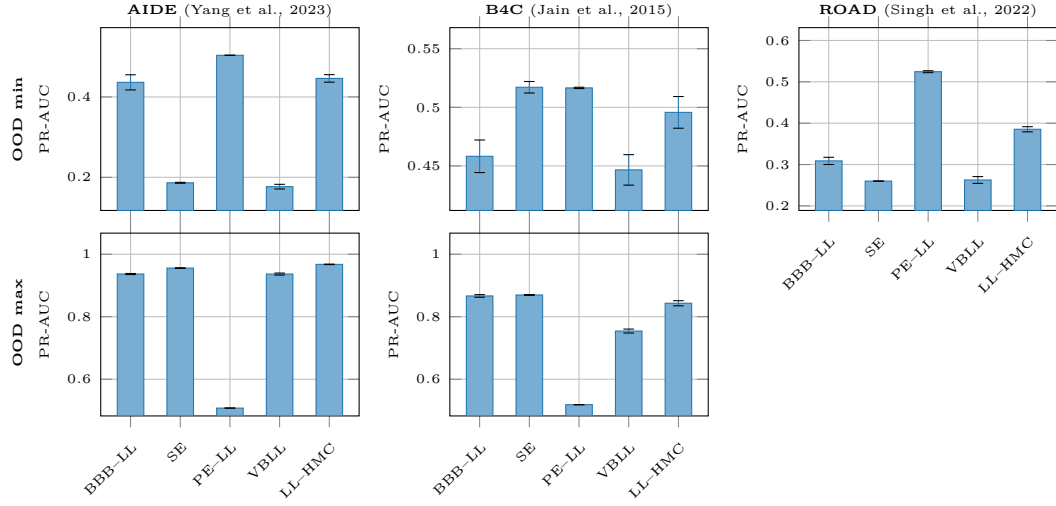


Figure 12: Average uncertainty-based OOD detection performance (PR-AUC) across the included LL-PDL methods for the best performing hyperparameter configuration across 100 random seeds.

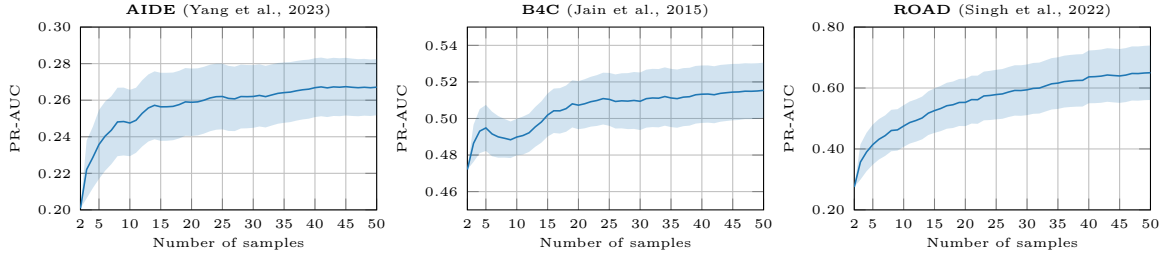


Figure 13: Effects of additional dependent samples from the same chain of the top-performing LL-HMC configuration for the OOD min scenario for different 100 random seeds. The light blue area illustrates the standard deviation of the cumulative of the PR-AUC for each additional sample.

Table 6: Average OOD top-performance and two standard errors of the mean across five random seeds for LL-HMC with multiple starting positions or chains. S=Starting Positions, C=Chains.

		AIDE (Yang et al., 2023)						B4C (Jain et al., 2015)						ROAD (Singh et al., 2022)					
		ROC-AUC (↑)	OOD min PR-AUC (↑)	FPR95 (↓)	ROC-AUC (↑)	OOD max PR-AUC (↑)	FPR95 (↓)	ROC-AUC (↑)	OOD min PR-AUC (↑)	FPR95 (↓)	ROC-AUC (↑)	OOD max PR-AUC (↑)	FPR95 (↓)	ROC-AUC (↑)	OOD min PR-AUC (↑)	FPR95 (↓)			
LL-HMC	S=1	C=1	0.90±0.01	0.52±0.01	0.21±0.02	0.95±0.00	0.99±0.00	0.14±0.01	0.83±0.01	0.70±0.01	0.41±0.03	0.91±0.01	0.97±0.00	0.39±0.05	0.86±0.01	0.73±0.02	0.36±0.05		
		C=2	0.91±0.03	0.58±0.10	0.18±0.05	0.95±0.00	0.98±0.00	0.15±0.00	0.85±0.04	0.73±0.05	0.36±0.08	0.85±0.04	0.73±0.05	0.36±0.08	0.87±0.01	0.72±0.01	0.31±0.04		
	S=2	C=1	0.64±0.03	0.35±0.02	0.97±0.03	0.89±0.03	0.97±0.01	0.40±0.18	0.85±0.01	0.70±0.02	0.34±0.03	0.90±0.01	0.96±0.01	0.42±0.06	0.38±0.05	0.39±0.01	1.00±0.00		
		C=2	0.66±0.07	0.35±0.01	0.89±0.21	0.88±0.01	0.97±0.00	0.42±0.06	0.85±0.00	0.70±0.02	0.34±0.03	0.89±0.01	0.96±0.00	0.39±0.06	0.50±0.06	0.42±0.01	0.99±0.01		

Influence of additional predictions or samples. Figure 11 visualizes the influence of additional samples or predictions for the best performing hyperparameter configurations from Table 5 for 10 random seeds for the different numbers of samples or predictions. The BBB-LL results for the OOD min scenarios for the AIDE and B4C datasets show a slight improvement with additional samples, but this trend is not visible for the other scenarios or for the ROAD dataset. Opposed to the results in Table 4, LL-HMC for 10 different random seeds for each number of samples does not yield the highest performance on average for all scenarios. Similar to the in-distribution results, there is no single LL-PDL method consistently performs better in all scenarios.

Comparing the best hyperparameter configurations. Figure 12 shows the average PR-AUC across 100 random seeds for the best hyperparameter configurations from Table 5. The OOD detection performance

of the PE-LL and SE is stable across scenarios, with average PR-AUC values comparable to those reported in Table 4. In contrast, BBB-LL and LL-HMC exhibit greater variability in average performance across seeds and configurations depending on the OOD scenario. Overall, evaluating the top-performing configurations across multiple seeds suggests that no single LL-PDL method consistently outperforms the others.

Influence of additional dependent LL-HMC samples. Figure 13 shows how additional samples from the same HMC chain affect PR-AUC performance. The results are based on the best-performing grid search configuration. Compared to the modest F1-score gains in Figure 8, PR-AUC improves slightly more with additional same-chain samples in the OOD min scenario. However, the PR-AUC improvement stabilizes with more samples.

Multiple chains and starting positions. Table 6 reports OOD detection performance using the top-performing grid search configuration across five seeds, comparing different numbers of HMC chains (C) and starting positions (S). LL-HMC with a single starting position consistently yields strong OOD detection performance across the datasets, regardless of the number of chains. In contrast, using two starting positions results in less consistent performance. Specifically, in the AIDE OOD min and ROAD OOD min scenarios, LL-HMC with two starting positions produces higher FPR95 values, indicating reduced reliability in distinguishing in- and out-of-distribution instances. This suggests LL-HMC’s performance is sensitive to the learned latent representations, especially in how they guide the initialization and exploration of posterior modes. As with the in-distribution classification performance, increasing the number of chains or starting positions does not consistently improve OOD detection, and in some cases degrades performance.

6 Discussion and Conclusion

We evaluated and explored the effectiveness of applying Hamiltonian Monte Carlo (HMC) sampling to the final layer of deep neural networks for video-based driver action and intention recognition. Applying HMC to sample the parameters of the last layer reduces the required computational cost compared to sampling the entire network. While last layer HMC (LL-HMC) benefits from the Markov-Chain Monte Carlo sampling ability to explore complex and potentially multi-modal posterior distributions for the last layer’s parameters, its reliance on fixed pre-trained representations comes at the cost of not capturing the uncertainty inherent in the feature extraction layers of a deep neural network (DNN). Furthermore, as already indicated by the toy example, increasing the number of posterior samples improves the uncertainty estimations but saturates after a certain point.

Compared to the softmax-based baseline, the last layer probabilistic deep learning (PDL) approaches demonstrated improved performance under specific hyperparameter settings. However, the classification and OOD detection results across grid searches yielded significantly lower performance compared to the best performance for a single grid search. The effect of additional predictions by evaluating the best performing hyperparameter configuration across 100 random seeds for each last layer PDL method and dataset showed that LL-HMC yields competitive results. Additional samples or predictions did not consistently enhance the in-distribution or OOD performance for the included last layer PDL approaches.

While driving action and intention recognition are examples of realistic safety-critical applications, last layer PDL approaches can also be applied in other domains. For example, to support human-robot interaction through action and intention recognition (Qi et al., 2024), elderly care (Pereira & Han, 2009), predictive maintenance (Benker et al., 2021; Nguyen et al., 2022), medical imaging (Zou et al., 2023), and fraud detection (Habibpour et al., 2023). These tasks require different modeling approaches, which could provide deeper insights into how the underlying model representations affect the last layer uncertainty estimation performance.

None of the last layer PDL methods were able to consistently identify all OOD instances when the most or least prevailing driving maneuvers were removed from the datasets. This raises broader considerations for the design of safety-critical systems such as advanced driver assistance and autonomous driving technologies. For instance, when a model predicts two maneuvers (e.g., ‘left turn’ vs. ‘U-turn’) with similar high confidence and low uncertainty, the system defaults to pick the class with the highest assigned confidence, despite the

potential overlap. In such a scenario, it could be interesting to see whether predicting sets (Hüllermeier et al., 2022; Wang et al., 2024a) of potential maneuvers improves the performance. More broadly, if PDL methods are unable to reliably flag all OOD scenarios, we should also consider the potential outcome of the recommendations given the current driving scene. By leveraging a more decision-theoretic approach that incorporates generic task knowledge (e.g., penalizing intended maneuvers that potentially harm other road users), we might be able to produce better and safer recommendations (Cobb et al., 2018).

References

- Taiga Abe, Estefany Kelly Buchanan, Geoff Pleiss, Richard Zemel, and John P Cunningham. Deep ensembles work, but are they necessary? *Advances in Neural Information Processing Systems*, 35:33646–33660, 2022.
- Julyan Arbel, Konstantinos Pitas, Mariia Vladimirova, and Vincent Fortuin. A primer on bayesian neural networks: review and debates. *arXiv preprint arXiv:2309.16314*, 2023.
- Anurag Arnab, Mostafa Dehghani, Georg Heigold, Chen Sun, Mario Lučić, and Cordelia Schmid. Vivit: A video vision transformer. In *Proceedings of the IEEE/CVF International Conference on Computer Vision*, pp. 6836–6846, 2021.
- Arsenii Ashukha, Alexander Lyzhov, Dmitry Molchanov, and Dmitry Vetrov. Pitfalls of in-domain uncertainty estimation and ensembling in deep learning. In *International Conference on Learning Representations*, 2020.
- Mohini P Barde and Prajakt J Barde. What to use to express the variability of data: Standard deviation or standard error of mean? *Perspectives in clinical research*, 3(3):113–116, 2012.
- Yoshua Bengio, Geoffrey Hinton, Andrew Yao, Dawn Song, Pieter Abbeel, Trevor Darrell, Yuval Noah Harari, Ya-Qin Zhang, Lan Xue, Shai Shalev-Shwartz, et al. Managing extreme ai risks amid rapid progress. *Science*, 384(6698):842–845, 2024.
- Maximilian Benker, Lukas Furtner, Thomas Semm, and Michael F Zaeh. Utilizing uncertainty information in remaining useful life estimation via bayesian neural networks and hamiltonian monte carlo. *Journal of Manufacturing Systems*, 61:799–807, 2021.
- Leonard Berrada, Sumanth Dathathri, Krishnamurthy Dvijotham, Robert Stanforth, Rudy R Bunel, Jonathan Uesato, Sven Gowal, and M Pawan Kumar. Make sure you’re unsure: A framework for verifying probabilistic specifications. *Advances in Neural Information Processing Systems*, 34:11136–11147, 2021.
- Michael Betancourt. A conceptual introduction to hamiltonian monte carlo. *arXiv preprint arXiv:1701.02434*, 2017.
- Eli Bingham, Jonathan P. Chen, Martin Jankowiak, Fritz Obermeyer, Neeraj Pradhan, Theofanis Karaletsos, Rohit Singh, Paul Szerlip, Paul Horsfall, and Noah D. Goodman. Pyro: Deep Universal Probabilistic Programming. *Journal of Machine Learning Research*, 2018.
- David M Blei, Alp Kucukelbir, and Jon D McAuliffe. Variational inference: A review for statisticians. *Journal of the American statistical Association*, 112(518):859–877, 2017.
- Charles Blundell, Julien Cornebise, Koray Kavukcuoglu, and Daan Wierstra. Weight uncertainty in neural network. In *International Conference on Machine Learning*, pp. 1613–1622. PMLR, 2015.
- Xavier Bouthillier, César Laurent, and Pascal Vincent. Unreproducible research is reproducible. In *International Conference on Machine Learning*, pp. 725–734. PMLR, 2019.
- Tianqi Chen, Emily Fox, and Carlos Guestrin. Stochastic gradient hamiltonian monte carlo. In *International conference on machine learning*, pp. 1683–1691. PMLR, 2014.
- Adam D Cobb and Brian Jalaian. Scaling hamiltonian monte carlo inference for bayesian neural networks with symmetric splitting. In *Uncertainty in Artificial Intelligence*, pp. 675–685. PMLR, 2021.

-
- Adam D Cobb, Stephen J Roberts, and Yarin Gal. Loss-calibrated approximate inference in bayesian neural networks. *arXiv preprint arXiv:1805.03901*, 2018.
- Yimian Dai, Fabian Gieseke, Stefan Oehmcke, Yiquan Wu, and Kobus Barnard. Attentional feature fusion. In *Proceedings of the IEEE/CVF winter conference on applications of computer vision*, pp. 3560–3569, 2021.
- Armen Der Kiureghian and Ove Ditlevsen. Aleatory or epistemic? Does it matter? *Structural safety*, 31(2): 105–112, 2009.
- Nikita Durasov, Nik Dorndorf, Hieu Le, and Pascal Fua. Zigzag: Universal sampling-free uncertainty estimation through two-step inference. *Transactions on Machine Learning Research*, 2024. ISSN 2835-8856.
- Gianni Franchi, Olivier Laurent, Maxence Leguéry, Andrei Bursuc, Andrea Pilzer, and Angela Yao. Make me a bnn: A simple strategy for estimating bayesian uncertainty from pre-trained models. In *Proceedings of the IEEE/CVF Conference on Computer Vision and Pattern Recognition*, pp. 12194–12204, 2024.
- Yarin Gal and Zoubin Ghahramani. Dropout as a Bayesian approximation: Representing model uncertainty in deep learning. *International conference on machine learning*, pp. 1050–1059, 2016.
- Jakob Gawlikowski, Cedrique Rovile Njiteucheu Tassi, Mohsin Ali, Jongseok Lee, Matthias Humt, Jianxiang Feng, Anna Kruspe, Rudolph Triebel, Peter Jung, Ribana Roscher, et al. A survey of uncertainty in deep neural networks. *Artificial Intelligence Review*, 56(Suppl 1):1513–1589, 2023.
- Patrick Gebert, Alina Roitberg, Monica Haurilet, and Rainer Stiefelhagen. End-to-end prediction of driver intention using 3D convolutional neural networks. In *2019 IEEE Intelligent Vehicles Symposium (IV)*, pp. 969–974. IEEE, 2019.
- Andrew Gelman and Donald B Rubin. Inference from iterative simulation using multiple sequences. *Statistical science*, 7(4):457–472, 1992.
- Charles J Geyer. Practical Markov Chain Monte Carlo. *Statistical science*, pp. 473–483, 1992.
- Charles J Geyer. Introduction to Markov chain Monte Carlo. *Handbook of Markov chain Monte Carlo*, 2011.
- Chuan Guo, Geoff Pleiss, Yu Sun, and Kilian Q Weinberger. On calibration of modern neural networks. In *International Conference on Machine Learning*, pp. 1321–1330. PMLR, 2017.
- Maryam Habibpour, Hassan Gharoun, Mohammadreza Mehdipour, AmirReza Tajally, Hamzeh Asgharnezhad, Afshar Shamsi, Abbas Khosravi, and Saeid Nahavandi. Uncertainty-aware credit card fraud detection using deep learning. *Engineering Applications of Artificial Intelligence*, 123:106248, 2023.
- James Harrison, John Willes, and Jasper Snoek. Variational bayesian last layers. *The Twelfth International Conference on Learning Representations*, 2024.
- Dan Hendrycks, Nicholas Carlini, John Schulman, and Jacob Steinhardt. Unsolved problems in ml safety. *arXiv preprint arXiv:2109.13916*, 2021.
- Matthew D Hoffman, David M Blei, Chong Wang, and John Paisley. Stochastic variational inference. *Journal of Machine Learning Research*, 2013.
- Matthew D Hoffman, Andrew Gelman, et al. The no-u-turn sampler: adaptively setting path lengths in hamiltonian monte carlo. *J. Mach. Learn. Res.*, 15(1):1593–1623, 2014.
- Eyke Hüllermeier and Willem Waegeman. Aleatoric and epistemic uncertainty in machine learning: An introduction to concepts and methods. *Machine learning*, 110(3):457–506, 2021.
- Eyke Hüllermeier, Sébastien Destercke, and Mohammad Hossein Shaker. Quantification of credal uncertainty in machine learning: A critical analysis and empirical comparison. In *Uncertainty in Artificial Intelligence*, pp. 548–557. PMLR, 2022.

-
- Pavel Izmailov, Sharad Vikram, Matthew D Hoffman, and Andrew Gordon Gordon Wilson. What are bayesian neural network posteriors really like? In *International conference on machine learning*, pp. 4629–4640. PMLR, 2021.
- Ashesh Jain, Hema S Koppula, Bharad Raghavan, Shane Soh, and Ashutosh Saxena. Car that knows before you do: Anticipating maneuvers via learning temporal driving models. In *Proceedings of the IEEE International Conference on Computer Vision*, pp. 3182–3190, 2015.
- Michael I Jordan, Zoubin Ghahramani, Tommi S Jaakkola, and Lawrence K Saul. An introduction to variational methods for graphical models. *Machine learning*, 37(2):183–233, 1999.
- Laurent Valentin Jospin, Hamid Laga, Farid Boussaid, Wray Buntine, and Mohammed Bennamoun. Hands-on Bayesian neural networks—a tutorial for deep learning users. *IEEE Computational Intelligence Magazine*, 17(2):29–48, 2022.
- Will Kay, Joao Carreira, Karen Simonyan, Brian Zhang, Chloe Hillier, Sudheendra Vijayanarasimhan, Fabio Viola, Tim Green, Trevor Back, Paul Natsev, et al. The kinetics human action video dataset. *arXiv preprint arXiv:1705.06950*, 2017.
- Diederik P Kingma and Max Welling. Auto-encoding variational bayes. *International Conference on Learning Representations*, 2014.
- Vignesh Kothapalli. Neural collapse: A review on modelling principles and generalization. *Transactions on Machine Learning Research*, 2023.
- Balaji Lakshminarayanan, Alexander Pritzel, and Charles Blundell. Simple and scalable predictive uncertainty estimation using deep ensembles. *Advances in neural information processing systems*, 30, 2017.
- Olivier Laurent, Adrien Lafage, Enzo Tartaglione, Geoffrey Daniel, Jean-marc Martinez, Andrei Bursuc, and Gianni Franchi. Packed ensembles for efficient uncertainty estimation. In *The Eleventh International Conference on Learning Representations*, 2023.
- Olivier Laurent, Emanuel Aldea, and Gianni Franchi. A symmetry-aware exploration of bayesian neural network posteriors. In *The Twelfth International Conference on Learning Representations*, 2024.
- Phillip Lippe. UvA Deep Learning Tutorials. <https://uvadlc-notebooks.readthedocs.io/en/latest/>, 2022.
- Ilya Loshchilov and Frank Hutter. Decoupled Weight Decay Regularization. In *International Conference on Learning Representations*, 2018.
- Will Maddern, Geoff Pascoe, Chris Linegar, and Paul Newman. 1 Year, 1000km: The Oxford RobotCar Dataset. *The International Journal of Robotics Research (IJRR)*, 36(1):3–15, 2017. doi: 10.1177/0278364916679498.
- Wesley J Maddox, Pavel Izmailov, Timur Garipov, Dmitry P Vetrov, and Andrew Gordon Wilson. A simple baseline for Bayesian uncertainty in deep learning. *Advances in Neural Information Processing Systems*, 32: 13153–13164, 2019.
- Andrey Malinin and Mark Gales. Predictive uncertainty estimation via prior networks. *Advances in neural information processing systems*, 31, 2018.
- Shireen Kudukkil Manchingal and Fabio Cuzzolin. Position: Epistemic artificial intelligence is essential for machine learning models to know when they do not know. *arXiv preprint arXiv:2505.04950*, 2025.
- Lassi Meronen, Martin Trapp, Andrea Pilzer, Le Yang, and Arno Solin. Fixing overconfidence in dynamic neural networks. In *Proceedings of the IEEE/CVF winter conference on applications of computer vision*, pp. 2680–2690, 2024.
- Grégoire Montavon, Mikio L Braun, and Klaus-Robert Müller. Kernel analysis of deep networks. *Journal of Machine Learning Research*, 12(9), 2011.

-
- Bálint Mucsányi, Michael Kirchhof, and Seong Joon Oh. Benchmarking uncertainty disentanglement: Specialized uncertainties for specialized tasks. *Advances in neural information processing systems*, 37: 50972–51038, 2024.
- Jishnu Mukhoti, Andreas Kirsch, Joost van Amersfoort, Philip HS Torr, and Yarin Gal. Deep deterministic uncertainty: A new simple baseline. In *Proceedings of the IEEE/CVF Conference on Computer Vision and Pattern Recognition*, pp. 24384–24394, 2023.
- Radford Neal. Bayesian learning via stochastic dynamics. *Advances in neural information processing systems*, 1992.
- Radford Neal et al. MCMC using hamiltonian dynamics. *Handbook of markov chain monte carlo*, 2011.
- Radford M Neal. *Bayesian learning for neural networks*. Springer Science & Business Media, 1996.
- Khanh TP Nguyen, Kamal Medjaher, and Christian Gogu. Probabilistic deep learning methodology for uncertainty quantification of remaining useful lifetime of multi-component systems. *Reliability Engineering & System Safety*, 222:108383, 2022.
- Jeremy Nixon, Michael W Dusenberry, Linchuan Zhang, Ghassen Jerfel, and Dustin Tran. Measuring calibration in deep learning. In *CVPR Workshops*, volume 2, 2019.
- Chihiro Noguchi and Toshihiro Tanizawa. Ego-vehicle action recognition based on semi-supervised contrastive learning. In *Proceedings of the IEEE/CVF Winter Conference on Applications of Computer Vision*, pp. 5988–5998, 2023.
- Theodore Papamarkou, Maria Skoularidou, Konstantina Palla, Laurence Aitchison, Julyan Arbel, David Dunson, Maurizio Filippone, Vincent Fortuin, Philipp Hennig, et al. Position: Bayesian deep learning is needed in the age of large-scale ai. In *Forty-first International Conference on Machine Learning*, 2024.
- Vardan Papayan, XY Han, and David L Donoho. Prevalence of neural collapse during the terminal phase of deep learning training. *Proceedings of the National Academy of Sciences*, 117(40):24652–24663, 2020.
- Fabian Pedregosa, Gaël Varoquaux, Alexandre Gramfort, Vincent Michel, Bertrand Thirion, Olivier Grisel, Mathieu Blondel, Peter Prettenhofer, Ron Weiss, Vincent Dubourg, et al. Scikit-learn: Machine learning in python. *the Journal of machine Learning research*, 12:2825–2830, 2011.
- Luís Moniz Pereira and The Anh Han. Elder care via intention recognition and evolution propection. In *International Conference on Applications of Declarative Programming and Knowledge Management*, pp. 170–187. Springer, 2009.
- Luis Moniz Pereira et al. State-of-the-art of intention recognition and its use in decision making. *AI Communications*, 26(2):237–246, 2013.
- Janis Postels, Mattia Segù, Tao Sun, Luca Daniel Sieber, Luc Van Gool, Fisher Yu, and Federico Tombari. On the practicality of deterministic epistemic uncertainty. In *International Conference on Machine Learning*, pp. 17870–17909. PMLR, 2022.
- Lorena Qendro, Alexander Campbell, Pietro Lio, and Cecilia Mascolo. Early exit ensembles for uncertainty quantification. In *Machine Learning for Health*, pp. 181–195. PMLR, 2021.
- Jing Qi, Li Ma, Zhenchao Cui, and Yushu Yu. Computer vision-based hand gesture recognition for human-robot interaction: a review. *Complex & Intelligent Systems*, 10(1):1581–1606, 2024.
- Yao Rong, Zeynep Akata, and Enkelejda Kasneci. Driver intention anticipation based on in-cabin and driving scene monitoring. In *2020 IEEE 23rd International Conference on Intelligent Transportation Systems (ITSC)*, pp. 1–8. IEEE, 2020.
- Cynthia Rudin. Stop explaining black box machine learning models for high stakes decisions and use interpretable models instead. *Nature machine intelligence*, 1(5):206–215, 2019.

-
- Fariba Sadri. Logic-based approaches to intention recognition. In *Handbook of research on ambient intelligence and smart environments: Trends and perspectives*, pp. 346–375. IGI Global, 2011.
- Glenn Shafer and Vladimir Vovk. A tutorial on conformal prediction. *Journal of Machine Learning Research*, 9(3), 2008.
- Gurkirt Singh, Stephen Akrigg, Manuele Di Maio, Valentina Fontana, Reza Javanmard Alitappeh, Suman Saha, Kossar Jeddisaravi, Farzad Yousefi, Jacob Culley, Tom Nicholson, et al. Road: The road event awareness dataset for autonomous driving. *IEEE Transactions on Pattern Analysis & Machine Intelligence*, 45(01):1–1, feb 2022. ISSN 1939-3539. doi: 10.1109/TPAMI.2022.3150906.
- Lewis Smith and Yarin Gal. Understanding measures of uncertainty for adversarial example detection. *arXiv preprint arXiv:1803.08533*, 2018.
- Jasper Snoek, Oren Rippel, Kevin Swersky, Ryan Kiros, Nadathur Satish, Narayanan Sundaram, Mostofa Patwary, Mr Prabhat, and Ryan Adams. Scalable Bayesian optimization using deep neural networks. In *International conference on machine learning*, pp. 2171–2180. PMLR, 2015.
- Sylvain Gugger, Lysandre Debut, Thomas Wolf, Philipp Schmid, Zachary Mueller, Sourab Mangrulkar, Marc Sun, Benjamin Bossan. Accelerate: Training and inference at scale made simple, efficient and adaptable. <https://github.com/huggingface/accelerate>, 2022.
- Zhan Tong, Yibing Song, Jue Wang, and Limin Wang. Videomae: Masked autoencoders are data-efficient learners for self-supervised video pre-training. *Advances in neural information processing systems*, 35: 10078–10093, 2022.
- Matias Valdenegro-Toro. Sub-ensembles for fast uncertainty estimation in neural networks. In *Proceedings of the IEEE/CVF International Conference on Computer Vision*, pp. 4119–4127, 2023.
- Joost Van Amersfoort, Lewis Smith, Yee Whye Teh, and Yarin Gal. Uncertainty estimation using a single deep deterministic neural network. In *International conference on machine learning*, pp. 9690–9700. PMLR, 2020.
- Koen Vellenga, H Joe Steinhauer, Alexander Karlsson, Göran Falkman, Asli Rhodin, and Ashok Chaitanya Koppisetty. Driver intention recognition: State-of-the-art review. *IEEE Open Journal of Intelligent Transportation Systems*, 2022.
- Koen Vellenga, Alexander Karlsson, H Joe Steinhauer, Göran Falkman, and Anders Sjögren. PT-HMC: Optimization-based pre-training with Hamiltonian Monte-Carlo sampling for driver intention recognition. *ACM Transactions on Probabilistic Machine Learning*, 2024a.
- Koen Vellenga, H Joe Steinhauer, Göran Falkman, and Tomas Björklund. Evaluation of video masked autoencoders’ performance and uncertainty estimations for driver action and intention recognition. In *Proceedings of the IEEE/CVF Winter Conference on Applications of Computer Vision*, pp. 7429–7437, 2024b.
- Kaizheng Wang, Fabio Cuzzolin, Keivan Shariatmadar, David Moens, and Hans Hallez. Credal wrapper of model averaging for uncertainty estimation in classification. In *The Thirteenth International Conference on Learning Representations*, 2024a.
- Yixuan Wang, Ruochen Jiao, Simon Sinong Zhan, Chengtian Lang, Chao Huang, Zhaoran Wang, Zhuoran Yang, and Qi Zhu. Empowering autonomous driving with large language models: A safety perspective. In *ICLR 2024 Workshop on Large Language Model (LLM) Agents*, 2024b.
- Joe Watson, Jihao Andreas Lin, Pascal Klink, Joni Pajarinen, and Jan Peters. Latent derivative Bayesian last layer networks. In *International Conference on Artificial Intelligence and Statistics*, pp. 1198–1206. PMLR, 2021.
- Max Welling and Yee W Teh. Bayesian learning via stochastic gradient langevin dynamics. In *Proceedings of the 28th international conference on machine learning (ICML-11)*, pp. 681–688. Citeseer, 2011.

-
- Andrew G Wilson and Pavel Izmailov. Bayesian deep learning and a probabilistic perspective of generalization. *Advances in neural information processing systems*, pp. 4697–4708, 2020.
- Dingkang Yang, Shuai Huang, Zhi Xu, Zhenpeng Li, Shunli Wang, Mingcheng Li, Yuzheng Wang, Yang Liu, Kun Yang, Zhaoyu Chen, et al. Aide: A vision-driven multi-view, multi-modal, multi-tasking dataset for assistive driving perception. In *Proceedings of the IEEE/CVF International Conference on Computer Vision*, pp. 20459–20470, 2023.
- Jingkang Yang, Kaiyang Zhou, Yixuan Li, and Ziwei Liu. Generalized out-of-distribution detection: A survey. *International Journal of Computer Vision*, 132(12):5635–5662, 2024.
- Ruqi Zhang, Chunyuan Li, Jianyi Zhang, Changyou Chen, and Andrew Gordon Wilson. Cyclical stochastic gradient mcmc for bayesian deep learning. *International Conference on Learning Representations*, 2020.
- Xinlei Zhou, Han Liu, Farhad Pourpanah, Tiejong Zeng, and Xizhao Wang. A survey on epistemic (model) uncertainty in supervised learning: Recent advances and applications. *Neurocomputing*, pp. 449–465, 2022.
- Ke Zou, Zhihao Chen, Xuedong Yuan, Xiaojing Shen, Meng Wang, and Huazhu Fu. A review of uncertainty estimation and its application in medical imaging. *Meta-Radiology*, 1(1):100003, 2023.

Appendices

A Intermediate latent representation performance

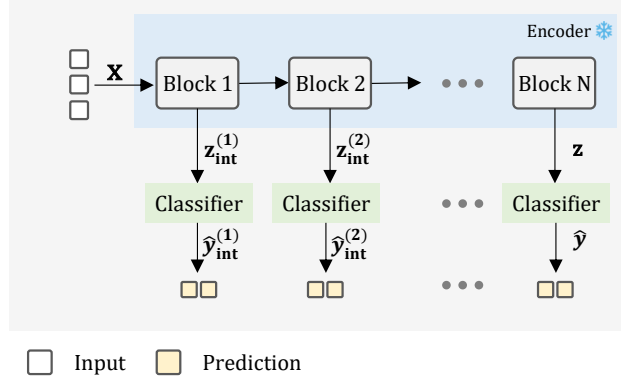


Figure 14: Schematic intermediate representation classification overview. The intermediate latent representation z_{int}^i can be extracted at different depths from the encoder, and used to produce intermediate classifications.

For deeper DNNs, previous studies have indicated that the intermediate latent representations can already be used to classify before the final layer of a network (Montavon et al., 2011; Pappan et al., 2020; Kothapalli, 2023) (see Figure 14). To reduce the required computations to produce uncertainty estimations further, Qendro et al. (2021) and Meronen et al. (2024) showed that using probabilistic last layers trained on these intermediate representations of a single network can improve the performance. Subsequently, these intermediate predictions can be incrementally used to create a model-internal ensemble, which combines the predictions from different depths of a network to improve the performance (Meronen et al., 2024). This potentially enables to not having to compute the entire network but to rely on intermediate representations for confident prediction and uncertainty estimation.

Processing a single 16-frame video requires approximately 361×10^9 floating point operations (FLOPs) for a ViT-Base model, where each Transformer block accounts for 29.8×10^9 FLOPs. Given the resource-constrained operating environment of DAR and DIR, and prior work highlighting the utility of intermediate representations for classification (Pappan et al., 2020; Qendro et al., 2021; Kothapalli, 2023; Meronen et al., 2024), we evaluate LL-PDL methods’ performance when trained on the representations extracted from the intermediate layers. We extract the latent features from each block via average pooling and apply the top-performing configurations to these intermediate features. Following (Qendro et al., 2021; Meronen et al., 2024), we assess whether predictions, either from individual layers or ensembles in the form of accumulated predictions from previous intermediate layers surpass the full network performance.

Results. Figure 15 illustrates the F1-score of the LL-PDL methods based on the intermediate latent representations of the ViT-Base model. For the AIDE and B4C datasets, the performance starts to saturate when relying on deeper latent representations, but never exceeds the final latent representation performance as reported in Table 1. For the ROAD dataset, the performance exhibits more variability, potentially due to the smaller dataset size. Only for the SE on the ROAD dataset, we observe improved performance based on the intermediate representation.

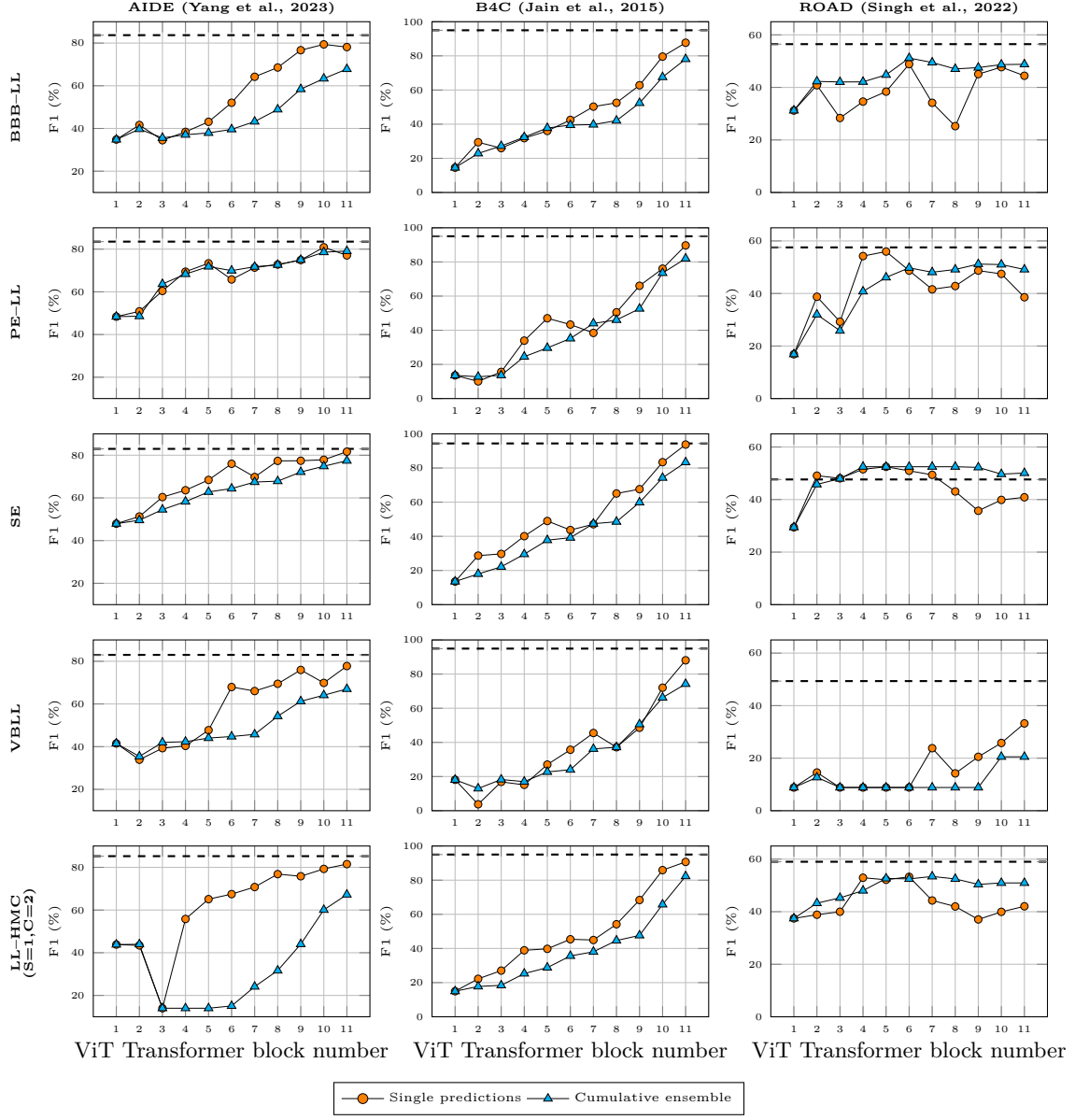


Figure 15: Performance overview for the single and cumulative ensembles based on the intermediate latent representations. The dashed lines indicate the best performance for each LL-PDL method performed on the final latent representation.